CZECH TECHNICAL UNIVERSITY IN PRAGUE

FACULTY OF NUCLEAR SCIENCES AND PHYSICAL ENGINEERING

Department of Physics
Experimental Nuclear and Particle Physics

BACHELOR THESIS

Azimuthal asymmetries in coherent photoproduction of J/ψ with ALICE

Vypracovala:	Sára Haidlová
Vedoucí práce:	prof. Jesús Guillermo Contreras Nuño, Ph.D
Rok:	2021

ČESKÉ VYSOKÉ UČENÍ TECHNICKÉ V PRAZE

FAKULTA JADERNÁ A FYZIKÁLNĚ INŽENÝRSKÁ

Katedra fyziky

Experimentální jaderná a částicová fyzika

BAKALÁŘSKÁ PRÁCE

Azimutální asymetrie v koherentní J/ψ fotoprodukci na experimentu ALICE

Vypracovala:	Sára Haidlová
Vedoucí práce:	prof. Jesús Guillermo Contreras Nuño, Ph.D
Rok:	2021

Katedra: fyziky

Akademický rok: 2020/2021

ZADÁNÍ BAKALÁŘSKÉ PRÁCE

Student: Sára Haidlová

Studijní program: Aplikace přírodních věd

Obor: Experimentální jaderná a částicová fyzika

Název práce: Azimutální asymetrie v koherentní J/Psi fotoprodukci na experimentu
(česky) ALICE

Název práce: Azimuthal asymmetries in coherent photoproduction of J/Psi with
(anglicky) ALICE

Pokyny pro vypracování:

1) Vypracování rešerše na téma:

- Dosavadní měření koherentní J/Psi fotoprodukce v midrapiditě na experimentu ALICE

- Azimutální asymetrie v ultra-periferálních srážkách

2) Studium azimutálních asymetrií v koherentní J/Psi fotoprodukci v midrapiditě na experimentu ALICE

Doporučená literatura:

[1] K. Aamodt, et al. (ALICE Collaboration): The ALICE experiment at the CERN LHC, JINST 3 (2008) S08002

[2] J.G. Contreras and J. D. Tapia Takaki: Ultra-peripheral heavy-ion collisions at the LHC, International Journal of Modern Physics A 30(8), 1542012 (2015)

[3] E. Abbas, et al. (ALICE Collaboration): Charmonium and e+e- pair photoproduction at mid-rapidity in ultra-peripheral Pb-Pb collisions at sqrt(s_(NN))=2.76 TeV, Eur.Phys.J. C73 (2013) no.11, 2617

Jméno a pracoviště vedoucího bakalářské práce:

prof. Jesus Guillermo Contreras, Ph.D., Katedra fyziky
Fakulta jaderná a fyzikálně inženýrská ČVUT v Praze

Jméno a pracoviště konzultanta:
Mgr. Michal Broz, Ph.D., Katedra fyziky
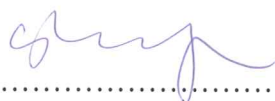Fakulta jaderná a fyzikálně inzenýrská ČVUT v Praze

Datum zadání bakalářské práce: 23.10.2020

Termín odevzdání bakalářské práce: 07.07.2021

Doba platnosti zadání je dva roky od data zadání.

....
garant oboru

....
vedoucí katedry

....
děkan

V Praze dne   23.10.2020

Prohlášení

Prohlašuji, že jsem svou bakalářskou práci vypracovala samostatně a použila jsem pouze podklady (literaturu, projekty, SW atd.) uvedené v přiloženém seznamu.

Nemám závažný důvod proti použití tohoto školního díla ve smyslu § 60 Zákona č.121/2000 Sb., o právu autorském, o právech souvisejících s právem autorským a o změně některých zákonů (autorský zákon).

V Praze dne ....
                                                                              Sára Haidlová

Acknowledgments

Abstrakt: Jeden z nejvíce studovaných problémů v kvantové chromodynamice je distribuce gluonů ve struktuře hadronů a jejich chování. Tyto distribuce mohou být studovány za použití ALICE na LHC pomocí exkluzivní J/ψ fotoprodukce. Často používané procesy pro fotoprodukci hadronů a studium hadronové struktury jsou ultra-periferní srážky, zejména vysoko-energetické ultra-periferní srážky. Tyto srážky nastávají pro impakt parametry větší než je suma poloměrů obou jader, což umožňuje kolize bez hadronických interakcí a nabité částice mohou interagovat pouze skrze svá elektromagnetická pole. Díky vysoké energii jsou distribuce studovány při nízkém Bjorken-x, pro které roste počet partonů a měření rozptylového úhlu J/ψ umožní další studium evoluce v Bjorken-x struktury hadronů. Analyzovaná data jsou z Pb-Pb srážek při $\sqrt{s_{NN}} = 5.02$ TeV. Nadějí je, že studium modulací v azimutálním úhlu umožní nový náhled do gluonové struktury hadronů.

Klíčová slova: QCD, UPC, J/ψ

Title:
Azimuthal asymmetries in coherent photoproduction of J/ψ with ALICE

Author:	Sára Haidlová

Study program:	Applied Natural Sciences
Specialization:	Experimental Nuclear and Particle Physics
Sort of project:	Bachelor thesis

Supervisor:	prof. Jesús Guillermo Contreras Nuño, Ph.D
	Department of Physics, Faculty of Nuclear Sciences and Physical Engineering, Czech Technical University in Prague
Consultant:	Mgr. Michal Broz, Ph.D.
	Department of Physics, Faculty of Nuclear Sciences and Physical Engineering, Czech Technical University in Prague

Abstract: One of the most studied problems in quantum chromodynamics is the gluon structure of hadrons and its behaviour. These distributions can be studied with ALICE at the LHC using exclusive J/ψ photoproduction. Processes frequently used for hadron photoproduction and studying the hadron structure are ultra-peripheral collisions (UPCs), specially high energy UPCs. These collisions occur for impact parameters larger than the sum of radii of nuclei, which allows for collisions where no hadronic interactions occur and charged particles interact through their electromagnetic fields. Given the large energy, the distributions are studied at low Bjorken-x, for which the number of partons rises and measurements of the scattering angle of the J/ψ allow for further studies of the evolution in Bjorken-x of the structure of hadrons. The analysed data are from Pb-Pb collisions at $\sqrt{s_{NN}} = 5.02$ TeV. There is hope that the study of modulations in azimuthal angle provides new insights into the hadron gluon structure.
Key words: QCD, UPC, J/ψ

Contents

List of Tables

List of Figures

Introduction

The current particle physics research allows us to study interactions and particles in a very small scale, allowing for probing and studying the most basic structures known to men. A theory used to describe some of these phenomena is quantum chromodynamics (QCD), which describes the behaviour of gluons and quarks, the basic hadron building blocks. The structure of hadrons can be described by parton distribution functions, that vary for different values of Bjorken-x. At the region of low Bjorken-x, the building blocks participating in the hadron structure are mostly gluons. The concept of parton distribution functions and the hadrons structure and needed theoretical background is described in Chapter 1 and Chapter 2. Furthermore in Chapter 2 the ultra-peripheral collisions are described. These collisions are a powerful tool for probing the gluon structure.

In Chapter 3 the ALICE detector at the CERN LHC is described, because it is used to measure photoproduction in ultra-peripheral collisions for high energies.

In Chapter 4 are mentioned two papers from previous research. One concerning the previous measurements of coherent and incoherent J/ψ photoproduction. The second paper introduces measurements of modulations in azimuthal angle in Breit-Wheeler process with high magnetic fields.

In the last chapter my own contribution is described. The data selection for exclusive coherent J/ψ photoproduction is presented and the steps on the analysis as well as the first preliminary results on the azimuthal asymmetries of J/ψ are presented.

The thesis ends with a short summary and an outlook of future work.

Chapter 1

The Standard Model

The Standard Model is a particle physics theory combining the electroweak theory describing electromagnetic and weak interactions and quantum chromodynamics describing the strong interaction. In addition the theory classifies elementary particles. The particles are divided into three groups given the spin of the particle: gauge bosons, fermions and the Higgs boson. In the following sections the four fundamental interactions and elementary particles will be introduced.

1.1 Particles

1.1.1 Properties of particles

Firstly several properties of elementary particles will be described. The first crucial property of particles measured in particle physics is the invariant mass. Invariant mass is defined by the relativistic formula shown in Eq. (1.1). The invariant mass is used to determine the rest mass of a decaying particle through measurements of the four momenta of its decay products.

$$M^2 c^4 = E^2 - p^2 c^2. \tag{1.1}$$

Another important property of particles is momentum. Momentum in relativistic physics can be separated into two parts, transversal p_T and longitudinal p_L. This separation can be done due to the relativistic transformations of momentum between frames. The transformation of a 4-vector is shown in Eq. (1.2), where β is the velocity between two reference frames, γ is the Lorentz boost, a prime distinguishes the energy (E) and momenta components along the x and y and z directions: p_x, p_y, p_z respectively. Given the transformation the momentum can be separated as $p_T = p_T(p_y, p_y)$, which is Lorentz invariant and $p_L = p_L(p_x)$ which is not Lorentz invariant. Given its invariance, the transversal momentum plays a key role in particle physics, as it can be measured with trackers immersed in a magnetic field or calculated from

transversal energy measured in calorimeters.

$$
\begin{aligned}
p'_x &= \gamma(p_x - \beta E), \\
p'_y &= p_y, \\
p'_z &= p_z, \\
E &= \gamma(E - \beta p_x).
\end{aligned}
\tag{1.2}
$$

Apart from classifying momentum given its behaviour in relativistic physics, it is important to mention transformations of coordinates used due to the geometry of an experiment or a situation. For collisions spherical coordinates are used. In spherical coordinates the momentum is expressed as a function of the polar and azimuthal angles, where the polar angle is an angle between the 3-momentum of a particle and the beam axis and the azimuthal angle is an angle in the plane transversal to the beam axis.

In particle physics it is common to use pseudorapidity as a spatial coordinate to describe the polar angle. Pseudorapidity is given by Eq. (1.3).

$$
\eta = -\ln\left[\tan\left(\frac{\theta}{2}\right)\right].
\tag{1.3}
$$

Pseudorapidity can also be given by Eq. (1.4), where p is the 3-momentum and p_L is the longitudinal momentum.

$$
\eta = \frac{1}{2}\left(\frac{|p| + p_L}{|p| - p_L}\right).
\tag{1.4}
$$

Another variable commonly measured in particle physics is rapidity. The rapidity is defined as Eq. (1.5), where E is the energy of a particle and p_z is the z component of the momentum of the particle. Rapidity is not Lorentz invariant, but is Lorentz additive, therefore the difference between rapidities is invariant along the beam axis.

$$
y = \frac{1}{2}\ln\frac{E + p_z c}{E - p_z c}.
\tag{1.5}
$$

As mentioned at the beginning of this chapter, the Standard Model divides particles into groups according to their spin. Spin is a property of a particle observed solely in quantum mechanics. Spin is defined as inner angular momentum and even though it does not have an analogy in classical physics, it is often compared to the angular momentum described in classical physics.

1.1.2 Leptons

The first group of particles mentioned in this thesis are leptons. Leptons are fermions (particles with half-integer spin) classified into 3 families. In each family there is a negatively charged particle and their corresponding neutral neutrinos. The charged particles are called electron, muon and tau. Given the fact that the electron, muon

and tau carry electric charge, they can interact via the electromagnetic interaction, whereas neutral neutrinos do not. Leptons do not carry colour charge, which prevents them from interacting via the strong interaction, therefore in general leptons interact via the electroweak interaction. Another important property of neutrinos is their low mass, according to the Standard Model the mass of neutrinos is even equal to zero.

1.1.3 Hadrons

Hadrons are particles composed of quarks and can be divided into two large groups called baryons and mesons. According to the quark model, there are predicted also tetraquarks, pentaquarks and glueballs.

1.1.3.1 Quarks

Quarks are fundamental particles in subatomic physics. Analogously to leptons, quarks can be found in three generations, the first generation is up and down quark, second is charm and strange and third is top and bottom. Quarks are particles with electric charge and what is more, the only particles known to carry non-integer electric charge. Apart from electric charge, quarks carry colour charge which allows them to interact via the strong interaction. The behaviour of quarks will be described in Chapter 2.

1.1.3.2 Baryons

Baryons are fermions composed of three quarks. The most known baryons are the proton and neutron. Both of those baryons interact via the electromagnetic, strong and weak interactions.

1.1.4 Mesons and J/ψ

Mesons are bosons composed of a pair of quark and antiquark. A meson of particular interest in this thesis is the J/ψ meson. The J/ψ meson is a vector meson composed of a charmed quark and an antiquark, which gives it charm number equal to zero even though the meson is composed of charm quarks. These mesons are known to have hidden charm. The J/ψ is a vector meson. Vector mesons are mesons with spin 1 and negative parity. The mass of the J/ψ is $M_{J/\psi} = (3.096916 \pm 0.000011)$ GeV/c^2 and the decay width $\Gamma_{J/\psi} = (92.9 \pm 2.8)$ keV [17]. The J/ψ does not have electric charge, therefore it does not interact primarily via the electromagnetic force and it can decay via the strong interaction. The main decay channels of J/ψ are hadronic with $(87.7 \pm 0.5)\%$ [17]. Other important decay channels are the leptonic channels $\mu^+ + \mu^-$ and $e^+ + e^-$ with probabilities $(5.961 \pm 0.033)\%$ and $(5.971 \pm 0.032)\%$ [17], respectively.

1.2 Interactions

In particle physics, the interaction of two particles can be described as the interaction of two fields via the superposition of two waves. This superposition creates envelopes that can be explained as virtual particles. These particles have different properties than real particles and time of their existence is given by the uncertainty relation defined as Eq. (1.6), where E is the energy of the particle, t is time and $\hbar$ is the reduced Planck constant.

$$\Delta E \Delta t \geq \frac{\hbar}{2}. \tag{1.6}$$

Different types of virtual particles and interactions are mentioned in the following subsections.

1.2.1 Electromagnetic interaction

The electromagnetic interaction is an interaction affecting particles with electric charge or magnetic momentum and is observable in classical physic with infinite reach. The strength of the interaction is given by the coupling constant $\alpha_{em} = \frac{1}{137}$. The virtual particle of the electromagnetic interaction is the massless photon with spin 1 and negative parity.

1.2.2 Weak interaction

The weak interaction is mediated by three bosons $W^\pm, Z^0$. Given their large masses the reach of the interaction is small in comparison with the rest of the fundamental interactions, approximately 10^{-3} fm. The weak interaction is responsible for beta decay and does not conserve all quantum numbers and symmetries. Its strength is around $\alpha \approx 10^{-7}$.

1.2.3 Strong interaction

The strong interaction is affecting particles with colour charge and is responsible for bonding quarks inside hadrons. Moreover it is responsible for bonding protons and neutrons inside atomic nucleus. The reach of the strong interaction is approximately 1 fm and its strength is $\alpha_s \approx 1$. The virtual particles mediating strong interactions are 8 gluons. Gluons have no mass, colour charge and no electric charge. Further properties of the strong interaction and gluons and their behaviour will be discussed in Chapter 2.

Chapter 2

Quantum chromodynamics

Quantum chromodynamics (QCD) proposed in 1973 is a particle physics theory of the strong interaction describing the behaviour of quarks and gluons. This quantum field theory is a non-abelian gauge theory with symmetry group SU(3). For purposes of this thesis only several properties of QCD will be discussed without deep mathematical background.

2.1   Colour charge and quark confinement

As mentioned before, the strong interaction affects only particles carrying colour charge. The idea of colour charge was introduced as an explanation for the existence of particles composed of three identical quarks. Particles described in quantum mechanics are in general described by wavefunctions. Given the fact that hadrons are composed of quarks, the wavefunction of hadrons depends on their position in space, spin and flavour. The product of these factors is shown in Eq. (2.1).

$$\psi_{TOT} = \psi_{SPACE} \times \psi_{SPIN} \times \psi_{FLAVOUR}. \tag{2.1}$$

For particles composed of three same quarks, the wavefunction will be symmetric under the interchange of any two quarks. However the symmetry of the wavefunction contradicts one of the fundamental principles of quantum mechanics, Pauli exclusion principle. The Pauli exclusion principle states that no two fermions with the same quantum numbers can occupy the same quantum state in the system. Therefore the wavefunction should be asymmetric under the interchange of any two quarks. As an explanation it was suggested that quarks carry another quark number, colour, which will be included in the overall wavefunction seen in Eq. (2.2).

$$\psi_{TOT} = \psi_{SPACE} \times \psi_{SPIN} \times \psi_{FLAVOUR} \times \psi_{COLOUR}. \tag{2.2}$$

So far the colour was interpreted as a quantum number, yet it can also be interpreted as a new type of charge with three values red, blue and green that can be used as the elements of the fundamental representation of SU(3). By a combination of colour and anticolour triplets two multiplets are generated. A colour octet that correspond to 8

gluons that change colour and a colour singlet that does not and so is not observable.

The introduction of colour charge led to the description of another phenomenon as well, the colour confinement. In the context of QCD confinement is described by saying that only bound states that exist have to have total colour quantum number equal to zero. These states are called colour singlets. Since only particles in colour singlets are observable, colour charged particles can not be observed in normal conditions.

2.2 Coupling constant and asymptotic freedom

Coupling constants in general determine the strength of the interaction. Several coupling constants were previously mentioned, for example for the electromagnetic interaction the coupling constant is $\alpha_{em} \approx 1/137$. In classical physics the electromagnetic force is given by Coulomb's law defined as Eq. (2.3).

$$F = k\frac{Z_1 e Z_2 e}{r^2}. \tag{2.3}$$

The strength of the electromagnetic force is given by the electric charge e. With decreasing distance between charges, the effects from quantum mechanics come into effect and must be taken into account. The electromagnetic interaction in the microscopic world is described by quantum electrodynamics and the strength of this interaction is given by the aforementioned coupling constant $\alpha_{em} \approx 1/137$. It was observed that the behaviour of this constant depends on the distance from which the interaction is observed. With smaller distance the coupling constant is larger.

Parallel phenomena was observed in QCD. The coupling constant for the strong interaction denoted $\alpha_s \approx 1$ as mentioned before. Similarly to the coupling constant in QED, the coupling constant in QCD was observed to be dependent on the distance from which it is observed, although the dependence is opposite, with decreasing distance the magnitude decreases. This observation is related to the above mentioned colour confinement. When it is attempted to separate two quarks it is needed to overcome a coupling constant of great magnitude. To separate the quarks it is needed to provide high enough energy that for the system it will be more energetically efficient to create a quark-antiquark pair from the vacuum, creating new colour neutral particles.

As mentioned, the coupling constant for the strong interaction decreases with distance. For very small distances the coupling constant becomes small enough that the chromodynamic forces between quarks disappear, and the theory can be considered asymptotically free.

This property of the coupling constant allows for the simplification of calculations in the form of perturbative QCD. Perturbative QCD uses known solutions of a simpler problem and adds corrections in the form of power series where the expansion parameter is α_s and this correction makes the transition to the uncomputable problem. The key condition is, that the expansion parameter is very small, which is met for small distances.

2.3 Screening

The behaviour of the coupling constants in QED and QCD is strongly related to a phenomenon called screening. When mentioning the coupling constant in QED, quantum mechanic effects were mentioned, these effects can be described as the polarisation of vacuum. The vacuum polarisation describes a processes where in the background of electric charge virtual electron-positron pairs are created. Positively charged positrons are attracted to the source of electric charge, for example an electron, and cover this "bare" charge.
This effect is afterwards seen when observing the dependence of the coupling constant on the observing distance. With greater distance the number of positrons covering the 'bare' charge which is the source of the interaction will be larger and the effective observed charge will be lower.

For QCD the vacuum can be considered to be a sea of quark-antiquark pairs and gluons and the same analogy can be applied for α_s. The colour charge is similarly to the electric charge 'dressed' in gluons and with larger distance more gluons are observed, which leads to the increase in the value of the observed effective charge.

2.4 Deep-inelastic scattering

Scattering processes have played a key role in the history of probing the structure of particles or nuclei. Starting with Rutherford's scattering experiments in good agreement with classical physics continuing with increasing energy of the probing particle and taking into account quantum-mechanical effects and ending with high energy probing the structure of hadrons. A good instrument for probing the structure of hadrons is deep-inelastic scattering (DIS).

Inelastic scattering in general means that the kinetic energy of the probing particle is not conserved. The adjective deep refers to the very high energy of the probing particle which causes the destruction of the hadron. This can be seen from the formula for de Broglie's wavelength defined by Eq. (2.4). With high momentum of the probe its wavelength will be very small, which allows for probing distances smaller in comparison with the dimensions of the target.

$$\lambda = \frac{h}{p}. \tag{2.4}$$

Depending on the used probe DIS can be divided into two classes, electroproduction and neutrinoproduction. The electroproduction uses electrons or muons, that are scattered of a hadron and involves single-photon or Z^0 exchange which indicates the presence of an electroweak interaction. The neutrinoproduction uses neutrinos and the scattering process involves the exchange of W^+ or Z^0 bosons which indicates the involvement of the weak interaction.

The main measurement of the experiments is the cross section and its dependencies on certain quantities. The cross section in a scattering processes is understood as an effective area for the collision, in DIS it is the effective area of the probed hadron.

The experiments measure the variation with the energy lost by the incoming lepton, which is given by the formula Eq. (2.5), where E_i represents the energy of the incoming lepton and E_f its energy after the scattering.

$$v = E_i - E_f. \tag{2.5}$$

Other dependency variable is the scattering angle θ. This angle is related to the transferred momentum and can be expressed by the formula defined in Eq. (2.6).

$$q^2 = 2E_i E_f (1 - \cos\theta). \tag{2.6}$$

Measuring of these observables provides a good way to connect data from the experiment with the theoretical predictions regarding the structure of hadrons. A good theoretical prediction on the structure of hadrons is given by the parton model proposed by Richard Feynman. The model simply states that hadrons are made up of constituents called partons. The model does not give any assumptions about partons and their properties are to be determined by experiments. A phenomenon that led to the validation of the parton model and allowed for a more profound understanding of the parton model and involved processes is called Bjorken scaling and will be mentioned in the following subsection.
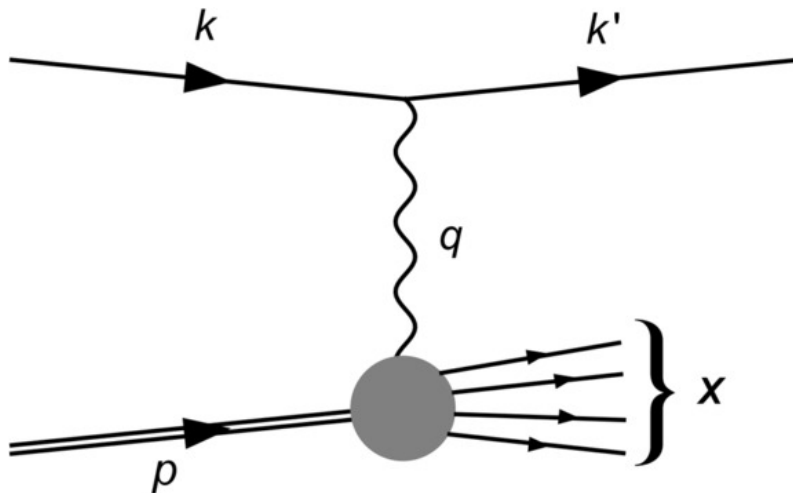
Figure 2.1: DIS of an electron (momentum k^μ) off a proton (momentum p^μ) [14].

2.4.1   Bjorken Scaling

The phenomenon called Bjorken scaling introduced by James Bjorken made predictions about cross sections in DIS depending on the magnitude of the momentum of the probe. If the momentum of the lepton scattering off the hadron becomes very large, than the formula for the cross section depending on the transferred energy and momentum squared becomes quite simple. This can be interpreted in the parton model mentioned above. With large probe momentum, the scattering off a hadron with finite diameter is replaced by the scattering off a point-like parton. The probe no longer scatters off the whole nucleon coherently and scatters off the individual partons incoherently. This phenomenon is expected to be observed when the wavelength of the probe is much less than the diameter of the hadron.

2.4.2 Structure functions

Previously it was mentioned that in DIS the main measurement is the measurement of the cross section. The cross section is composed of several factors each describing a different section of the interaction. For a better description let's suppose the example of DIS shown in Fig. 2.1. Whereas factors describing the propagation of particles participating in the reaction are given by quantum electrodynamics and thus are easily calculated, the vertex of the virtual photon and the hadronic current is unknown and it can be described using structure functions.

The form of the structure functions is determined by experiments and the functions are dependent on the previously mentioned variables v and q^2. Given the possible polarisation states of the virtual photon, longitudinal and transversal, there are two corresponding structure functions $F_1(q^2, v), F_2(q^2, v)$. The structure functions are solely factors without dimension, therefore dimensions of variables inside these functions must be cancelled out. This problem in high-energy physics was solved by James Bjorken by defining the dimensionless variable Bjorken-x defined by Eq. (2.7), where m_n is the nucleon mass. Bjorken accounted for very low wavelength of the probe, thanks to which the probe ceases to interact with the hadron as a whole and interacts solely with its small part of the hadron. With this variable in mind, structure functions are dependent solely on Bjorken-x for high values of momentum. The Bjorken-x variable can also be used to describe the distribution of momentum amongst partons inside hadrons.

$$x = \frac{q^2}{2m_n v}. \tag{2.7}$$

With further and more precise experiments with higher transferred momentum it was observed, that the dependence of structure functions is more complex. When studying the structure functions, the functions varied also with the transferred momentum, such a dependence can be observed in Fig. 2.2. As seen in Fig. 2.2, with higher Bjorken-x the number of partons decreases, which would suggest that one of the partons carries a greater part of the target momentum. But as known from the theory of quark confinement, this situation can be observed very briefly, until it is compensated by the strong interaction. With increasing transferred momentum and thus better resolution it can be observed that the number of partons with high Bjorken-x decreases even further and the number of partons with low Bjorken-x rises. Therefore with better resolution we may study more complicated QCD processes.

2.4.3 Saturation

Another key process regarding structure functions and QCD can be observed from studying the parton distribution functions of the proton. As it is known from the QCD theory, the quarks are glued together by an exchange of gluons, which causes probabilistic distributions over x. The behaviour of these distributions can be seen in Fig. 2.3. The graph shows the expected rise of parton distribution functions for low Bjorken-x as discussed above. As seen from the graph, the observed partons at low Bjorken-x are virtual quark-antiquark pairs and gluons. This confirms the
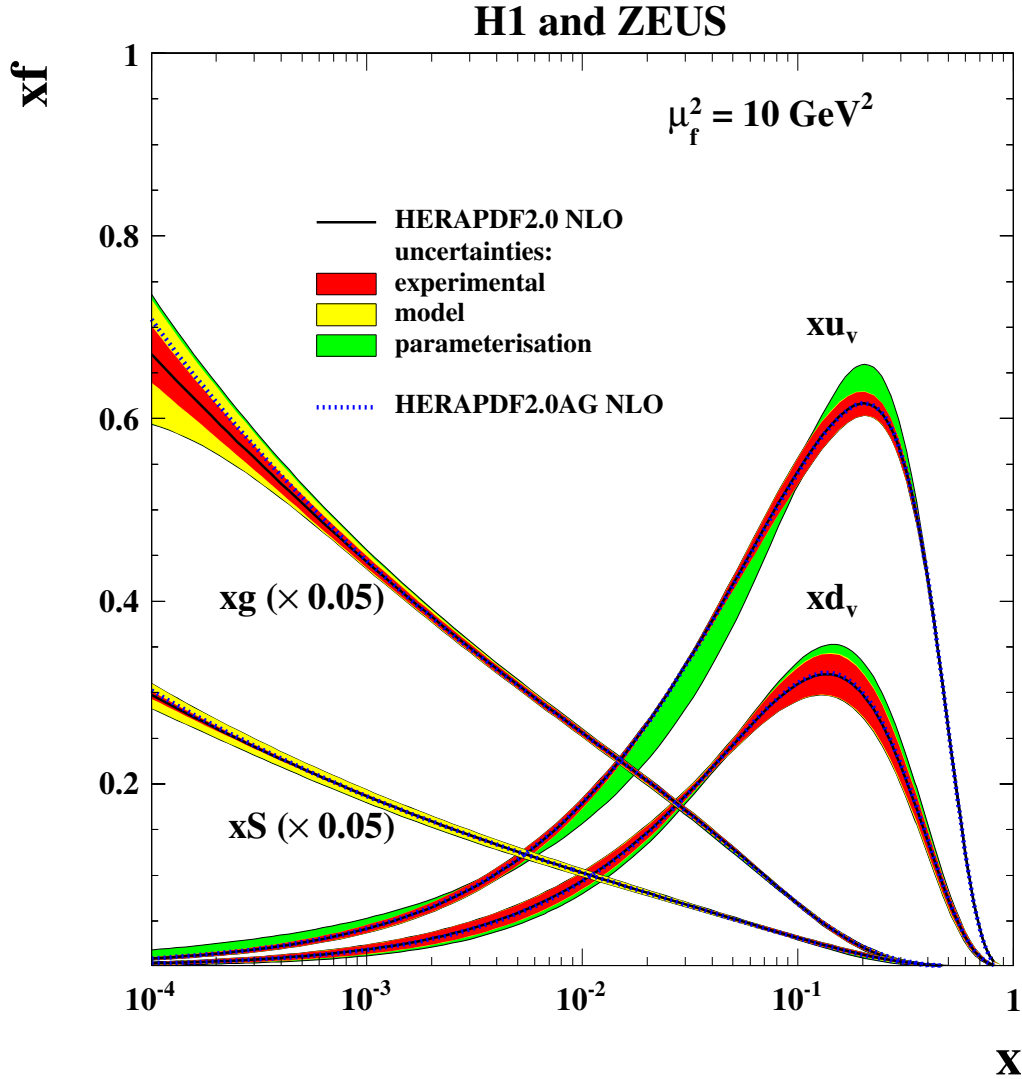
Figure 2.2: The parton distribution functions xu_v, xd_v, $xS = 2x(\bar{U} + \bar{D})$ and xg of HERAPDF2.0 NLO at $\mu_f^2 = 10\,\mathrm{GeV}^2$. The gluon and sea distributions are scaled down by a factor of 20. The experimental, model and parameterisation uncertainties are shown. [9].

previously mentioned assumption, that better resolution allows one to study complex QCD processes. With an increasing value of the transferred momentum the rise in the sea quark and gluon distribution would increase and it would to grow up to a number of gluons and sea quarks whose total cross section would be higher than the cross section. The phenomenon preventing this to happen is called saturation. Saturation states, that for a given value of Bjorken-x and lower, the gluons and sea quarks would recombine into partons with higher value of Bjorken-x.

2.5 Ultra-peripheral collisions

Ultra-peripheral collisions (UPCs) are used to probe the gluon distribution inside nuclei. Furthermore UPCs are widely used for hadron photoproduction and determination of hadron's quark content and spin structure or meson spectroscopy. UPCs
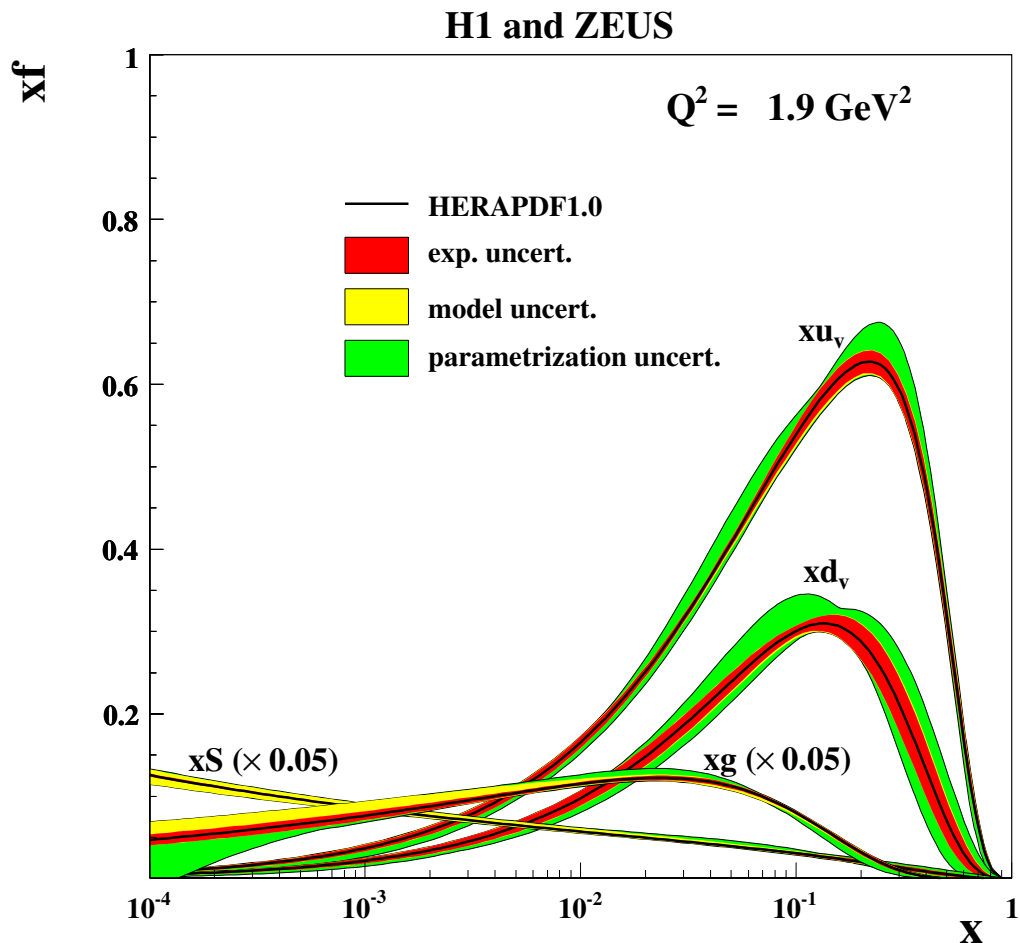
Figure 2.3: The parton distribution functions xu_v, xd_v, gluon distribution function xg and sea distribution function xS. The gluon and sea distributions are scaled down by a factor of 20. The transferred momentum is $Q^2 = 1.9$ GeV^2 [11].

are also a key instrument to test QED and electrodynamic processes in QCD.

Collisions may be classified according to their centrality, that is closely related to the impact parameter. The impact parameter is defined as the perpendicular distance between the centre of the target and the trajectory of the probing particle. Collisions with impact parameter equal to zero are classified as central collisions, peripheral collisions are those with impact parameter lower than, but close to, the sum of the radii of the particles and finally collisions with impact parameter larger than the sum of the radii are called ultra-peripheral collisions. Figure 2.4 shows schematics of an UPC.

2.5.1 Photoproduction

As mentioned before, UPCs are widely used for hadron or meson photoproduction. Ultra-relativistic charged particles have a radial electric field around them and a magnetic field circling it. As the particle gets accelerated, the electromag-
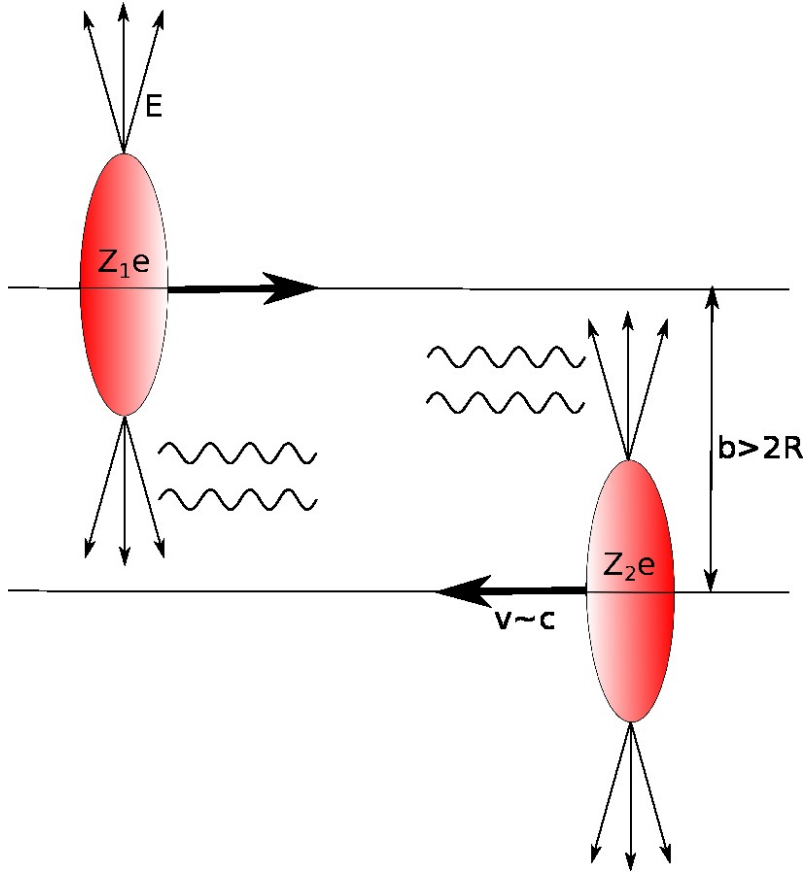
Figure 2.4: The schematics of the UPC [19].

netic field gets contracted by Lorentz transformation and thus flattens. According to Weizsäcker and Williams, this electromagnetic field can be interpreted as a flux of virtual photons. During UPCs no hadronic interactions occur given the large impact parameter and particles may interact only through the exchange of virtual photons. The virtual photon from the incoming particle may interact with the other particle or photons from each particle interact with each other.

The number of photons in the photon flux depends on the nuclear charge and the energy of the photons depends on the Lorentz contraction. The photon flux per unit area in the semi-classical description is given by Eq. (2.8) [10], where k is the energy of the photon in the frame of nucleus with Lorentz boost γ, Z is the nuclear charge and K_0, K_1 are Bessel functions. The variable x is defined as $x = kb/\gamma$.

$$n(k, \mathbf{b}) = \frac{\alpha Z^2}{\pi^2 b^2} x^2 \left[K_1^2(x) + \frac{1}{\gamma} K_0^2(x) \right]. \tag{2.8}$$

2.5.1.1 Exclusive vector meson production

In photoproduction the photon of the incident particle may fluctuate into a quark-antiquark pair that subsequently scatters off a target and emerges most likely as a vector meson. That is given by the spin and parity of photons. This process may be either coherent or incoherent. The coherent production involves the photon interaction with the whole nucleus. The coherent production can be further separated

into coherent production with or without nuclear break-up. If the photon interacts incoherently, it means it does not interact with the whole nucleus but only with its constituents. In this thesis the exclusive J/ψ photoproduction is of particular interest, which means that only a J/ψ is created without any other particles.

As previously mentioned the photon can either interact with the target nucleus or two photons may interact with each other. Both of those processes have been studied at the LHC up to now. The cross section for the photoproduction of a vector meson in UPC of Pb-Pb is given by Eq. (2.9) [10], where M is the mass, y is the rapidity and $\sigma_{\gamma Pb}(y)$ is the photoproduction cross section. The formula also uses $N_{\gamma/Pb}(y, M)$, which is the photon flux from a Pb nucleus and can be obtained from Eq. (2.8).

$$\frac{d\sigma_{PbPb}(y)}{dy} = N_{\gamma/Pb}(y, M)\sigma_{\gamma Pb}(y) + N_{\gamma/Pb}(-y, M)\sigma_{\gamma Pb}(-y). \qquad (2.9)$$

The produced vector meson has transverse momentum depending on the type of the production. For coherent production, the transverse momentum must be of the order of 0.5 $\hbar/R_{Pb}$, that corresponds to approximately 60 MeV/c [10]. For incoherent production the transverse momentum reaches values around 300 MeV/c [10].

Similarly to the formula of the cross section for the photoproduction of a vector meson in Pb-Pb collisions, one can write a formula for the cross section in p-Pb collisions defined as Eq. (2.10) [10].

$$\frac{d\sigma_{pPb}(y)}{dy} = N_{\gamma/Pb}(y, M)\sigma_{\gamma Pb}(y). \qquad (2.10)$$

Depending on whether the proton with which the photon interact stays intact or dissociates, the transverse momenta of the produced systems are of the order of 300 MeV/c [10] and 1 GeV/c [10] respectively.

The created J/ψ is measured solely through its decay products, mainly dilepton pairs. Apart from the previously mentioned collisions, two photon interaction also contribute to the J/ψ signal. The cross section for such process is given by Eq. (2.11) [4], where β is the velocity of the lepton in the rest frame of the two photons.

$$\sigma_{\gamma\gamma} = \frac{\pi\alpha^2}{4s}\beta\left[\frac{3-\beta^4}{2\beta}\ln\frac{1+\beta}{1-\beta} - 2 + \beta^2\right]. \qquad (2.11)$$

Chapter 3

The ALICE detector at the LHC

ALICE, short for A Large Ion Collider Experiment, is a general-purpose heavy-ion detector at the CERN LHC. CERN is an organisation focusing on nuclear research located in Geneva, Switzerland. ALICE was designed to study the strong interactions in matter; that is to study QCD. The experiment focuses on the physics of the quark-gluon plasma, a state of matter produced at extremely high energy densities and temperatures [1].

With 23 member states from Europe CERN provides scientific facilities such as particle accelerators for research in high-energy physics. Since founded in 1954, CERN has contributed vastly to the development of technology and science, including the discovery of neutral currents or new particles, such as W, Z and Higgs bosons. Furthermore, the World-Wide Web was invented at CERN. Throughout time CERN facilities developed resulting in the development of numerous types of accelerator and research facilities including the Large Hadron Collider (LHC) [3]. A schematic of the CERN's accelerator complex is shown in Fig. 3.1

3.1   The Large Hadron Collider

The LHC, located up to 100 metres underground and having 27 km in perimeter, is currently the largest particle accelerator in the world used to accelerate protons and heavy ions. The ring uses superconducting electromagnets and structures for particle acceleration working in a superconducting state, needing temperatures lower than outer space. Inside the tunnel are located two beam pipes kept at ultra high vacuum, in which the two particle beams travel before they collide.

Before reaching the LHC a particle is primarily accelerated it is send to radio frequency quadrupoles (QRF), which are used for further acceleration and focusation of the particle beam. Futhermore, given its composition, the QRFs create bunches. After being accelerated up to 750 keV [7], the beam is sent to a linear accelerator, where it is accelerated up to 50 MeV [7]. Afterwards it is sent to the Proton Synchrotron Booster (PSB), where the beam is accelerated to 1.4 GeV and is subsequently injected in the Proton Synchroton (PS). The PS accelerates the particles
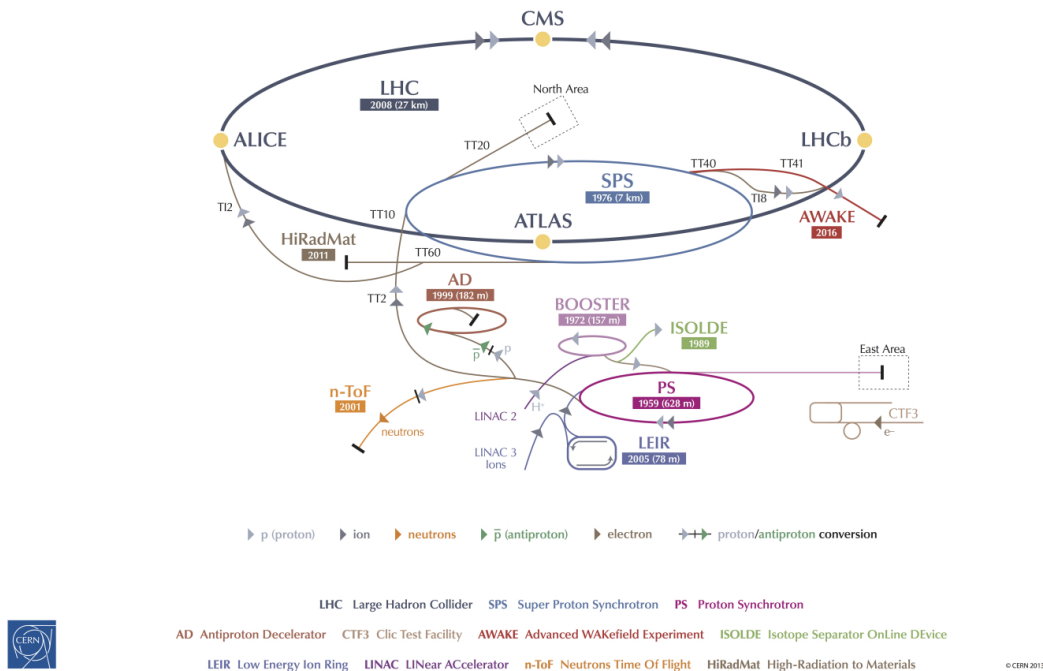
Figure 3.1: CERN's accelerator complex [12].

to 26 GeV and sends bunches to the Super Proton Synchrotron (SPS) accelerator, which accelerates particles up to 450 GeV and injects them into the LHC [7].

The first operational run at the LHC happened on 20th November 2009. During Run 1, which continued to into early 2013, the LHC achieved 4 TeV per beam. The data from this first run lead to the discovery of Higgs boson. After the first run followed a two year long shutdown, until the 5th of April 2015, when the second operational run started, during which it was achieved 6.5 TeV per beam. Run 2 was followed by the second long shutdown starting in December 2018 and ending in 2021 [20].

3.2   ALICE

The detector itself with dimensions of 16×16×26 m^3 weights circa 10 000 t and is placed underground close to the St. Genis-Pouilly village in France [1]. The detector consists of multiple sub-systems and sub-detectors. In the centre of the detector is a barrel used for measurements of electrons, photons and hadrons; in addition there is a muon spectrometer. The central barrel is placed in a solenoid magnet reused from the L3 experiment at LEP.

The barrel consists of the Inner Tracking System (ITS), the Time-Projection Chamber (TPC), the Time-of-Flight (TOF) detector, the Ring Imaging Cherenkov (HMPID) detector and the Transition Radiation (TRD) detector as well as two electromag-

netic calorimeters (PHOS, EMCal). Other detectors cover the forward (backward) regions; for example the zero-degree calorimetres (ZDC), the V0 or the ALICE Diffractive (AD) detectors. For the purposes of this thesis only some of them are mentioned in detail. Furthermore, a crucial part of measurements are data acquisition and triggers, which will be also mentioned [18]. The complete schematic layout of the ALICE apparatus is shown in Fig. 3.2.
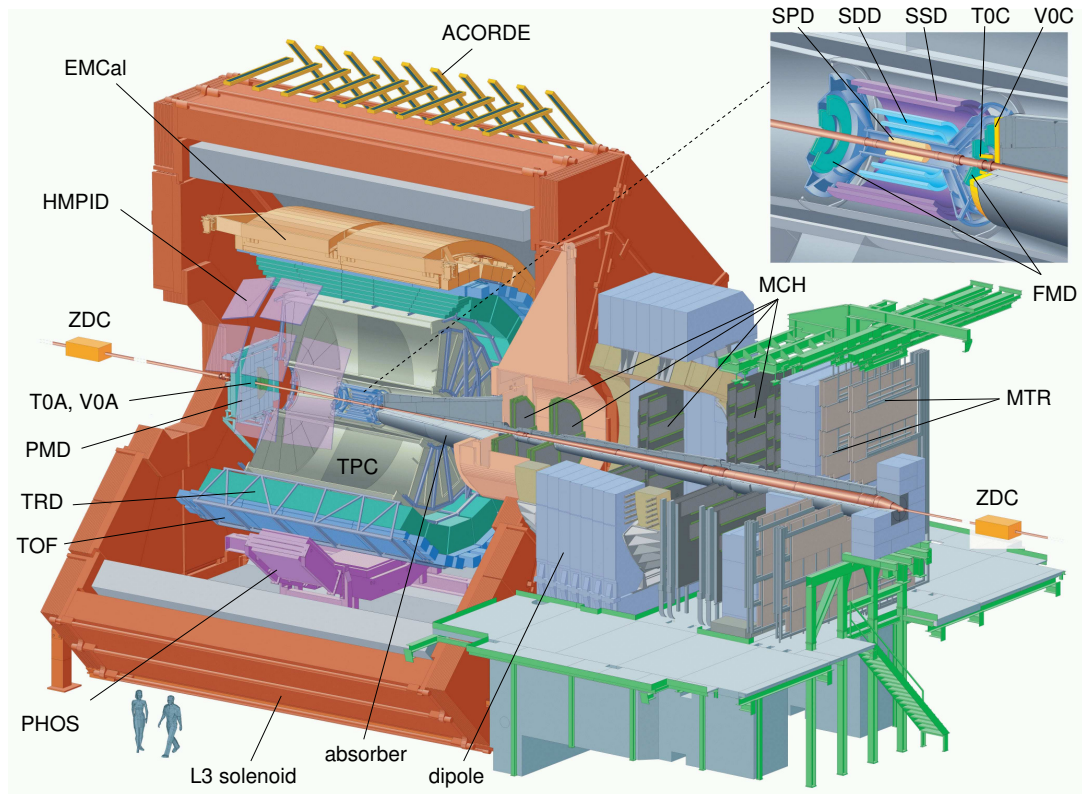
Figure 3.2: Schematics of the ALICE apparatus during the Run 1 at the LHC [18].

3.2.1 The Inner Tracking System

The first part of the central barrel described in this paper is the Inner Tracking System (ITS). The ITS, surrounding the beam pipe, is composed of six layers of silicon detectors with high precision (resolution better than 100 μm), which are used for primary and secondary vertex reconstruction and identifying and tracking particles with low momentum (bellow 200 MeV/c). All of the ITS layers are cylindrically shaped and coaxial with each other with radii between 4 and 43 cm. The ITS covers the pseudorapidity of $|\eta| < 0.9$ for vertices located ± 5.3 cm along the beam direction. The first two layers are the Silicon Pixel Detectors (SPD) followed by the Silicon Drift Detectors (SDD) and the Silicon micro-strip Detectors (SSD) for the last two layers of the ITS. The SDD and SSD detectors have analogue readout and are used for the measurement of the ionisation energy loss, dE/dx, in the non-relativistic region allowing to identify particles [15]. The distribution of the energy-loss signal in the ITS as a function of momentum is shown in Fig. 3.3. Numerical values in the following ITS description are taken from [18].
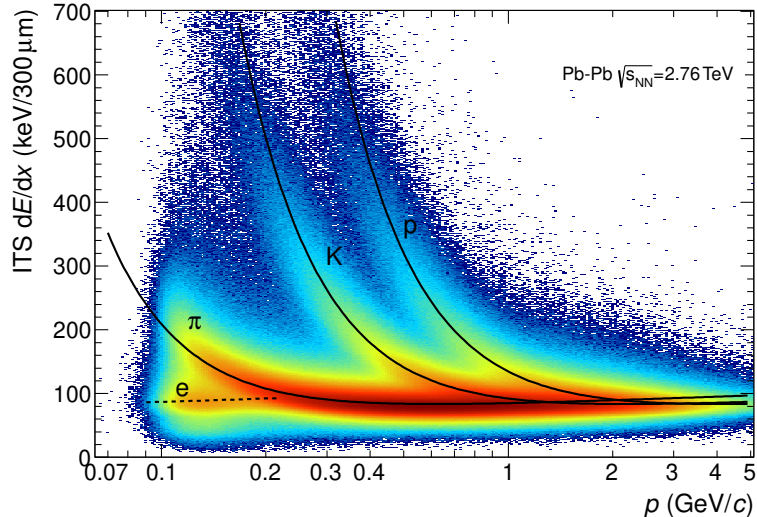
Figure 3.3: Distribution of the energy/loss signal in the ITS as a function of momentum. Both the energy loss and momentum are measured by the ITS alone [18].

3.2.1.1 The Silicon Pixel Detector

The two innermost layers of the ITS, the SPDs, are used to determine the position of the primary vertex and for the measurement of the distance of closest approach (DCA) of individual tracks to the primary vertex. The SPD uses hybrid silicon pixels and its inner radius is given by the radius of the beam pipe. The hybrid silicon pixel detectors are based on the combination of silicon detector diodes bump-bonded to readout chips with binary readout depending on a given treshold. This type of detector was chosen to provide sufficient DCA resolution for the high particle density expected in Pb-Pb collisions (50 particles/cm^2). The pseudorapidity coverage of the SPD is $|\eta| < 1.4$.

3.2.1.2 The Silicon Drift Detector

The SDDs are used to identify particles. In the two intermediate layers of the ITS the predicted charged particle density goes up to 7 particles/cm^2 and they provide half of the samples needed for the particle identification by the ITS. These detectors were made of high-resistivity silicon and their sensitive area is divided into two drift regions using a central cathode strip, each region carrying nearly 300 cathode strips.

3.2.1.3 The Silicon Strip Detectors

The double sided SSDs are used to complete the dE/dx measurement for particle identification via the ITS and are significant for the track-matching from the TPC to the ITS.

3.2.2 The Time Projection Chamber

The main tracking detector is the TPC [1]. The TPC is used for measurements of track momenta, particle identification and to determine vertices.
Given the expected maximum hit density, the inner radius of the chamber is 85 cm, the outer radius is 2.5 m. Given this outer radius the resolution for $\mathrm{d}E/\mathrm{d}x$ is better than 5-7% and covers the pseudorapidity area of $|\eta| < 1.5$ for a third of radial track length and $|\eta| < 0.9$ for the maximal radial track length; the TPC has full azimuth coverage. The transverse momentum is covered from 0.1 GeV/c to 100 GeV/c with sufficient resolution.

The detector is composed of a cylindrical field cage filled with a special gas mixture. Figure 3.4 shows a diagram of the TPC and its components. The field cage is designed to create a uniform electrostatic field and is operated with a voltage of 100 kV resulting in a maximum drift time of approximately 90 μs. The gas mixture is optimised for stability and ageing properties, low diffusion, low radiation length and the drift speed of the liberated electrons passing toward the end plates of the detector. The gas mixture is circulated and purified.
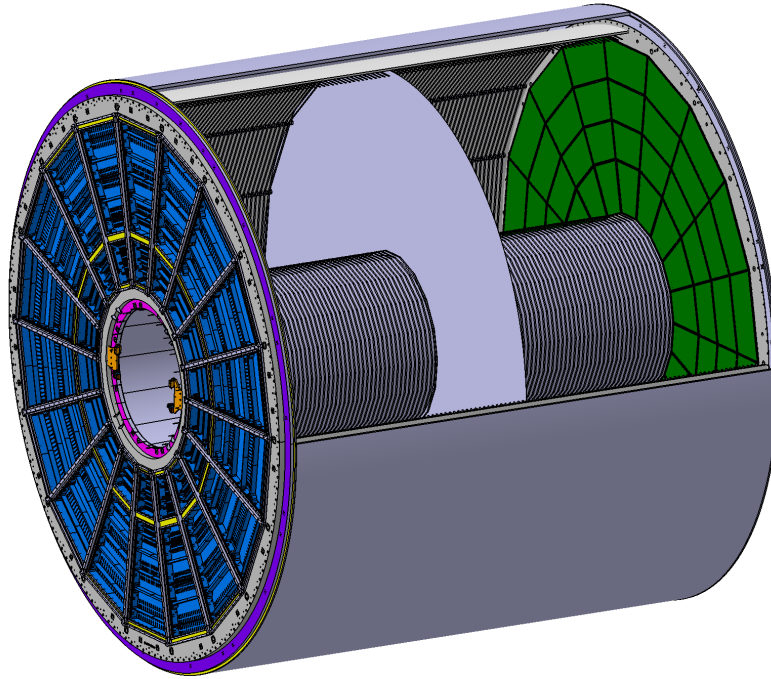
Figure 3.4: Overview of the ALICE TPC [6].

The two endplates of the cylindrical chamber cover an area of 32.5 m^2. These readout chambers are made of multi-wire proportional chambers and are segmented radially due to the radial dependence of the track density.

3.2.3 The Time-of-flight detector

The information used in this subsection is obtained from [1]. The time-of-flight detector is used in combination with the previously mentioned detectors for particle

identification by measuring the time of flight of the particle over a given distance yielding the velocity of a particle. The particle identification is in the intermediate momentum range between 2.5 GeV/c to 4 GeV/c for pions, kaons and protons. The detector covers the pseudorapidity $|\eta| < 0.9$. The internal radius of the detector is 370 cm and external is 399 cm.

The TOF is composed of MRCP strips placed inside modules acting like Faraday cages, positioned transversely to the beam direction. The overall length of an active region of the detector is 741 cm.

3.2.4   The V0 detector

The V0 detector consists of the V0A and V0C scintillator counters, V0A being placed 340 cm from the vertex opposite to the muon spectrometer and V0C placed 90 cm from the vertex on the front face of the hadronic absorber. The detectors cover the pseudorapidity range $2.8 < |\eta| < 5.1$ and $-3.7 < |\eta| < -1.7$ for V0A and V0C, respectively. The detectors are subdivided into 32 counters distributed into 4 rings. The scintillating material used in the V0 detector is BC404 with different thickness for each subdetector (2.5 cm for V0A and 2.0 cm for V0C) with WLS fibres with 1 mm in diameter.

The V0 detector can be used as a minimum-bias trigger for detectors located in the central barrel. V0 can serve as an indicator of centrality of the collision via the recorded multiplicity. Finally it is used for luminosity measurements [16].

3.2.5   The Zero Degree Calorimeter

In ALICE two sets of ZDCs are used to measure the energy of non-interacting nucleons (spectator nucleons) which yields the overlap region of the collision. Each set is located at 113 m on either side of the interaction point and is composed of two separate detectors each for a different spectator nucleon. The detectors for spectator protons are located between the beam pipes and the detectors for spectator protons are placed externally to the outgoing beam pipe. When not being used, the detectors can be lowered out of the horizontal plane of the beam [18].

3.2.6   The ALICE Diffractive detector

The ALICE Diffractive detector (AD detector) was installed during the Long Shutdown 1, after the Run 1 to increase ALICE sensitivity to diffractive masses. The sensitivity is close to the diffraction threshold of 1.08 GeV/c^2 [13]. It is made of two scintillating detectors. Each of them consists of 8 cells of plastic arranged around the beam pipe. As mentioned before, there are two detectors, ADA and ADC, covering the pseudorapidity interval $4.8 < \eta < 6.3$ and $-7.0 < \eta < -4.9$ [13] for ADA and ADC respectively. The light produced in scintillators is collected and transferred to optical fibers and via those fibres it is send to photo-multiplier tubes and converted

into an electric pulse. The AD detector not only expanded the pseudorapidity coverage of the minimum-bias triggers, but can be further used as a veto trigger for UPC events.

3.2.7 The Data acquisition system

The information mentioned in this subsection is obtained from [1]. A crucial part of data acquisition are triggers. Triggers are used to select the events we are interested in given their physics properties. Triggers used for ALICE need to be optimised for runs with different counting rates. To cope even with the highest multiplicities in Pb-Pb collisions, the so called fast part of the trigger is split into two levels, the signal from the first of them (Level 0) reaches the detector at 1.2 μs and receive only some trigger inputs, the second (Level 1) reaches the detector at 6.5 μs picking up the remaining outputs. The last level of trigger (Level 2) arriving at 88 μs is used to ensure the events are not spoilt by pile-up.
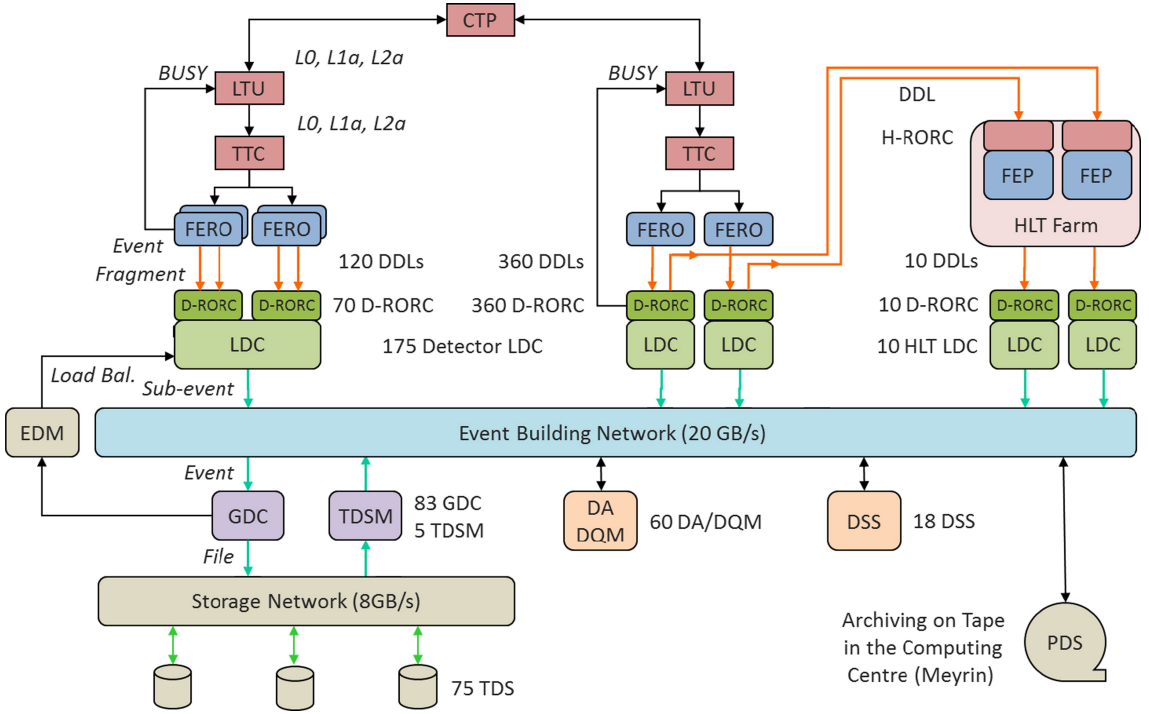
Figure 3.5: Overview of the hardware structure [8].

DAQ uses different trigger classes separated in two categories depending on their frequency. Operating in these two modes (frequent events with small amount of particles and rare events with high number of particles) is the Data AcQuisition System (DAQ). The layout of the DAQ is shown in Figure 3.5. Firstly the CTP sends out signals using the Local Trigger Unit (LTU) and the Timing, Trigger and Control system (TTC). Event fragments produced by the detectors are transfered by the Front-End Read-Out (FERO) electronics connected to Detector Data Links (DDL).

The measured data are sent afterwards to the DAQ readout Receiver Cards (D-RORC) which are connected to Local Data Concentrators (LDCs) and writes them

into LDCs memory, which subsequently assembles them into sub-events. LDCs then moves these sub-events to Global Data Collectors (GDCs), a farm of machines, for a whole event build. The availability of GDCs is broadcasted by an Event-Destination Manager (EDM). Apart from collecting sub-events and building full events, the GDCs send data to the recording system ending in Permanent Data Storage (PDS).

The high-Level Trigger system receives a copy of all relevant data using DDLsHLT Readout Receiver Card (H-RORC) into Front-End Processors (FEP). The HLT is composed of six layers. During data collection (first layer) the data is calibrated and hits and clusters get extracted. In the following layer the events are reconstructed for each detector and the fourth layer reconstructs the whole event. In layer 5 are selected events or regions regarding specific physics criteria. Lastly the data is compressed using complex algorithms.

Chapter 4

Previous measurements

In this chapter results of two papers are presented. The first paper studies charmonium and e^+e^- pair photoproduction at mid-rapidity in ultra-peripheral Pb-Pb collisions at $\sqrt{s_{NN}} = 2.76$ TeV, whereas the other one focuses on probing extreme electromagnetic fields with the Breit-Wheeler process while studying modulations in azimuthal angle in e^+e^- pair production. Apart from asymmetries mentioned herein, the $\cos 2\Delta\phi$ azimuthal asymmetry was also reported on preliminary results on ρ^0 meson production in ultra-peripheral heavy ion collisions.

4.1 Charmonium and e^+e^- pair photoproduction at mid-rapidity in ultra-peripheral Pb-Pb collisions at $\sqrt{s_{NN}} = 2.76$ TeV

In this section the results of charmonium and e^+e^- pair photoproduction at mid-rapidity in ultra-peripheral Pb-Pb collisions at $\sqrt{s_{NN}} = 2.76$ TeV are presented [2].

This paper studies exclusive, both coherent and incoherent, photoproduction of J/ψ (and ψ') mesons at mid-rapidity in the interval $|y| < 0.9$ and studies the region $x \approx 10^{-3}$ of gluon distributions. In addition, the paper explores the two-photon production of dilepton pairs and the influence of the large $Z\sqrt{\alpha}$ on the importance of higher-order terms in quantum electrodynamics calculations.

The analysed events were selected via a dedicated barrel ultra-peripheral trigger (BUPC) from the 2011 Pb-Pb data-taking. The trigger was set to select events with two tracks in an otherwise empty detector with the following properties:

- at least two hits in the SPD detector;

- a number of fired pad-OR (N^{on}) in the TOF detector in the range $2 \leq N^{on} \leq 6$, with at least two of them with a difference in azimuth, $\Delta\phi$, in the range $150° \leq \Delta\phi \leq 180°$;

- no hits in the VZERO-A and no hits in the VZERO-C detectors.

Using this criteria a total of approximately 6.5×10^6 events were selected. A visible cross section from van der Meer scans of $\sigma = 4.10^{+0.22}_{-0.13}$ (sys.) b, an integrated luminosity $\mathcal{L}_{int} = 23.0^{+0.7}_{-1.2} \mu\text{b}^{-1}$ was determined.

For the analysis were used the following selection criteria:

- a number of reconstructed tracks $1 \leq N_{TRK} \leq 10$, where a track is defined with loose criteria;

- a reconstructed primary vertex;

- only two good tracks passing tighter quality cuts;

- at least one of the two good tracks selected in the previous criterion with $p_T \geq 1$ GeV (this cut is used to reduce the background without affecting the genuine leptons from the J/ψ decay;

- the VZERO trigger required no signal within a time window of 25 ns around the collision time in any of the scintillator tiles of both VZERO-A and VZERO-C;

- the dE/dx of the two tracks is compatible with that of electrons or muons;

- the two tracks have the same or opposite charges, depending on the analysis;

- invariant mass $2.2 < M_{inv} < 6$ GeV/c^2.

Using these criteria 4,542 events were selected out of 6,507,692 triggered events. Moreover, by applying a cut $p_T < 200$ MeV/c for dimuons and $p_T < 300$ MeV/c for dielectrons on a first sample, enriched with coherent events, the number of events after this selections is reduced by 2.5% to 764 dielectron and 1301 dimuon coherent lepton-pair events. A second sample was enriched with incoherent events by applying a cut $p_T > 200$ MeV/c on dimuons and $p_T > 300$ MeV/c on dielectrons reducing the number to 278 electron and 1748 muon incoherent events.

A large number of coherent and incoherent J/ψ events (satisfying the previous characteristics) for the calculation of acceptance and efficiency was generated by STARLIGHT simulation. The obtained average results for the combined acceptance and efficiency for J/$\psi \rightarrow e^+e^- (\mu^+\mu^-)$ were 2.5% for coherent J/ψ in the dielectron channel and 1.0% for the dimuon channel and 6.5% for incoherent J/psi in the dielectron channel and 3.5% for the dimuon channel.

The invariant mass distribution is shown in Fig. 4.1 for both opposite-sign and like-sign electron and muon pairs. The J/ψ yield was obtained by fitting the invariant mass spectrum with an exponential function and a Crystal Ball function for the description of the underlying continuum and the J/ψ signal, respectively.

The yield obtained for the coherent sample is $N_{yield} = 265 \pm 40$ (sta.)± 12 (sys.) for the J/$\psi \rightarrow e^+e^-$ channel and $N_{yield} = 291 \pm 18$ (sta.) ± 4 (sys.) for the J/$\psi \rightarrow \mu^+\mu^-$ channel. The systematic error on the signal extraction is $^{+7\%}_{-6\%}$ for the dielectron channel and $^{+6\%}_{-5\%}$ for the dimuon channel. The total number of coherent J/ψs is calculated using Eq. (4.1), where f_D is the fraction of coherent J/ψ mesons coming
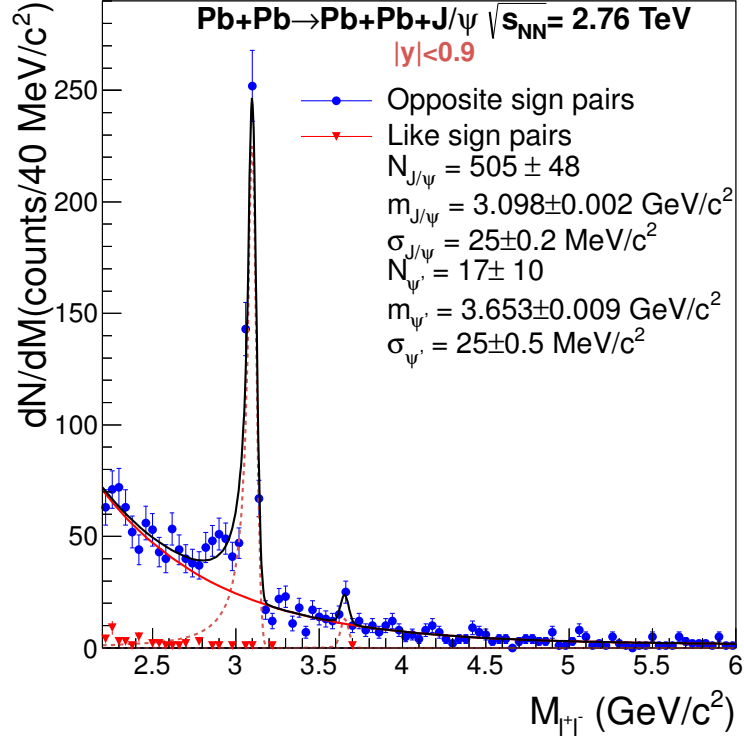
Figure 4.1: Invariant mass distribution for both opposite-sign and like-sign electron and muon pairs [2].

from $\psi' \to J/\psi$ + anything decay, f_I is the fraction of incoherent over coherent events in the low p_T region.

$$N_{J/\psi}^{coh} = \frac{N_{yield}}{1 + f_I + f_D}. \tag{4.1}$$

Results obtained by these calculations are $N_{J/\psi}^{coh}(\mu^+\mu^-) = 255 \pm 16 \text{ (sta.)}_{-13}^{+14} \text{ (sys.)}$ and $N_{J/\psi}^{coh}(\mu^+\mu^-) = 212 \pm 32 \text{ (sta.)}_{-13}^{+14} \text{ (sys.)}$.

Finally the coherent J/ψ differential cross section is given by Eq. (4.2).

$$\frac{d\sigma_{J/\psi}^{coh}}{dy} = \frac{N_{J/\psi}^{coh}}{(Acc \times \epsilon)_{J/\psi} \cdot BR(J/\psi \to l^+l^-) \cdot \mathcal{L}_{int} \cdot \Delta y}. \tag{4.2}$$

Using the values discussed before and the rapidity bin size interval $\Delta y = 1.8$ were obtained results $d\sigma_{J/\psi}^{coh}/dy = 2.27 \pm 0.14\text{(sta.)}_{-0.20}^{+0.30}\text{(sys.)}$ and $d\sigma_{J/\psi}^{coh}/dy = 3.19 \pm 0.50\text{(sta.)}_{-0.31}^{+0.45}\text{(sys.)}$ for dimuon and dielectron channels respectively. The weighted average gives $d\sigma/dy = 2.38_{-0.24}^{+0.34}\text{(sta. + sys.)}$ mb.

Results for the incoherent enriched sample, obtained by a similar way, are $N_{yield} = 61 \pm 14 \text{ (sta.)}_{-7}^{+16} \text{ (sys.)}$ for the J/$\psi \to e^+e^-$ channel and $N_{yield} = 91 \pm 15 \text{ (sta.)}_{-5}^{+7}$ (sys.) for the J/$\psi \to \mu^+\mu^-$ channel. The total number of incoherent events are $N_{J/\psi}^{inc}(\mu^+\mu^-) = 81 \pm 13 \text{ (sta.)}_{-6}^{+8} \text{ (sys.)}$ and $N_{J/\psi}^{inc}(e^+e^-) = 39 \pm 9 \text{ (sta.)}_{-5}^{+10} \text{ (sys.)}$. Those results correspond to $d\sigma/dy_{J/\psi}^{inc} = 1.03 \pm 0.17 \text{ (sta.)}_{-0.12}^{+0.15} \text{ (sys.)}$ mb and $d\sigma/dy_{J/\psi}^{inc} = 0.87 \pm 0.20 \text{ (sta.)}_{-0.14}^{+0.26} \text{ (sys.)}$ mb for dimuon and dielectron channels respectively. The weighted average gives $d\sigma/dy = 0.98_{-0.17}^{+0.19} \text{ (sta. + sys.)}$ mb.

Source	Coherent	Incoherent	$\gamma\gamma$ (low)	$\gamma\gamma$ (high)
Luminosity	$^{+5\%}_{-3\%}$	$^{+5\%}_{-3\%}$	$^{+5\%}_{-3\%}$	$^{+5\%}_{-3\%}$
Trigger dead time	$\pm2.5\%$	$\pm2.5\%$	$\pm2.5\%$	$\pm2.5\%$
Signal extraction	$^{+7\%}_{-6\%}\left(^{+6\%}_{-5\%}\right)$	$^{+26.5\%}_{-12.5\%}\left(^{+9\%}_{-8\%}\right)$	$\pm1\%$	$\pm4\%$
Trigger efficiency	$^{+3.8\%}_{-9.0\%}$	$^{+3.8\%}_{-9.0\%}$	$^{+3.8\%}_{-9.0\%}$	$^{+3.8\%}_{-9.0\%}$
(Acc $\times\ \varepsilon$)	$\pm2.5\%\ (\pm1\%)$	$\pm6.5(\pm3.5)\%$	$\pm0.3\%$	$\pm0.5\%$
$\gamma\gamma \to e^+e^-$ background	$^{+4\%}_{-0\%}$	$^{+4\%}_{-0\%}$	$^{+4\%}_{-0\%}$	$^{+4\%}_{-0\%}$
e/μ separation	$\pm2\%$	$\pm2\%$	$\pm1.7\%$	$\pm4\%$
Branching ratio	$\pm1\%$	$\pm1\%$	-	-
Neutron number cut	$^{+2.5\%}_{-0\%}$	-	-	-
Hadronic J/ψ	-	$^{+0\%}_{-5\%}\left(^{+0\%}_{-3\%}\right)$	-	-
Total	$^{+14.0\%}_{-9.6\%}\left(^{+13.4\%}_{-8.8\%}\right)$	$^{+29.4\%}_{-16.6\%}\left(^{+14.5\%}_{-11.7\%}\right)$	$^{+10.8\%}_{-7.0\%}$	$^{+12.0\%}_{-8.8\%}$

Table 4.1: Summary of the contributions to the systematic error for the J/ψ and $\gamma\gamma$ cross section measurement for electrons (muons). The error for the J/ψ signal extraction includes the systematic error in the fit of the invariant mass spectrum and the systematic errors on f_D and $f_I(f_C)$, as described in the text [2].

The yield $N^{e^+e^-}_{\gamma\gamma} = 186 \pm 13$ (sta.) ± 4 (sys.) was obtained by fitting in the invariant mass interval $2.2 < M_{inv} < 2.6$ GeV/c^2 and $N^{e^+e^-}_{\gamma\gamma} = 93 \pm 10$ (sta.) ± 4 (sys.) in the invariant mass interval $3.7 < M_{inv} < 10$ GeV/c^2 to avoid contamination from the J/ψ peak. The acceptance and efficiency for the lower invariant mass interval was calculated as 5.6% and 4.73% for the higher invariant mass interval. This result in $\sigma^{e^+e^-}_{\gamma\gamma} = 154 \pm 11$ (sta.)$^{+17}_{-11}$ μb and $\sigma^{e^+e^-}_{\gamma\gamma} = 91 \pm 10$ (sta.)$^{+11}_{-8}$ μb for the lower and higher invariant mass intervals respectively.

The summary of the contributions to the systematic error of all the calculated cross sections can be seen in Tab. 4.1. The measured cross sections for coherent photoproduction are compared with six different models in Fig. 4.2 and the cross section for incoherent photoproduction are compared with three different models in Fig. 4.3.
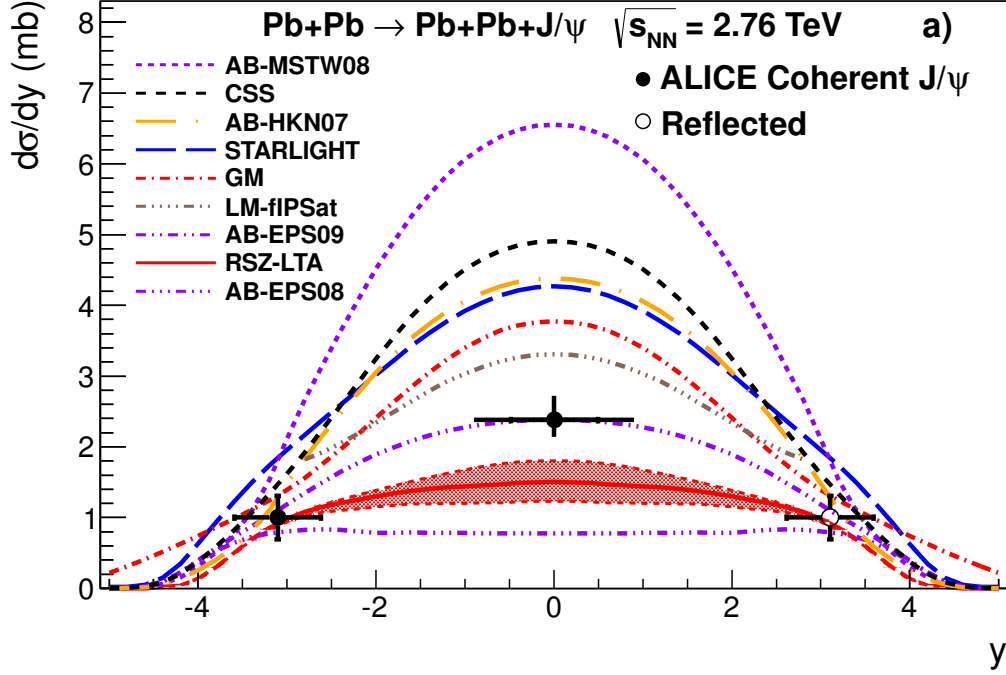
Figure 4.2: Measured differential cross section of J/ψ photoproduction in ultra-peripheral Pb-Pb collisions at $\sqrt{s_{NN}}$ = 2.76 TeV at -0.9 < y < 0.9 for coherent events. The error is the quadratic sum of the statistical and systematic errors. The theoretical calculations are also shown [2].

4.2 Probing Extreme Electromagnetic Fields with the Breit-Wheeler Process

In this section the results of probing extreme electromagnetic fields with the Breit-Wheeler Process are presented [5].

This paper studies measurements of exclusive e^+e^- pairs conducted by the STAR Collaboration at the Relativistic Heavy Ion Collider using in total $\sim$23$\times$10^6 Au-Au collisions at $\sqrt{s_{NN}}$ = 200 GeV corresponding to an integrated luminosity of 697 ± 70 μb^{-1} in year the 2010. These pairs are created through the Breit-Wheeler processes, which is a processes where two photons collide while creating an e^+e^- pair. Requirements for the experiment proposed by Breit and Wheeler, heavy nuclei and large impact parameter were satisfied by using Au-Au UPCs.

The expected features of the exclusive Breit-Wheeler process in ultra-relativistic heavy-ion collisions are listed bellow:

- Detection of e^+e^- pairs without accompanying background particles.

- Observation of a smooth e^+e^- invariant mass distribution without structure even in the mass range of known vector meson particles since the quantum numbers of two real photons (helicity state of 0 is disallowed) forbid the formation of a vector meson while highly virtual photons allow such a production
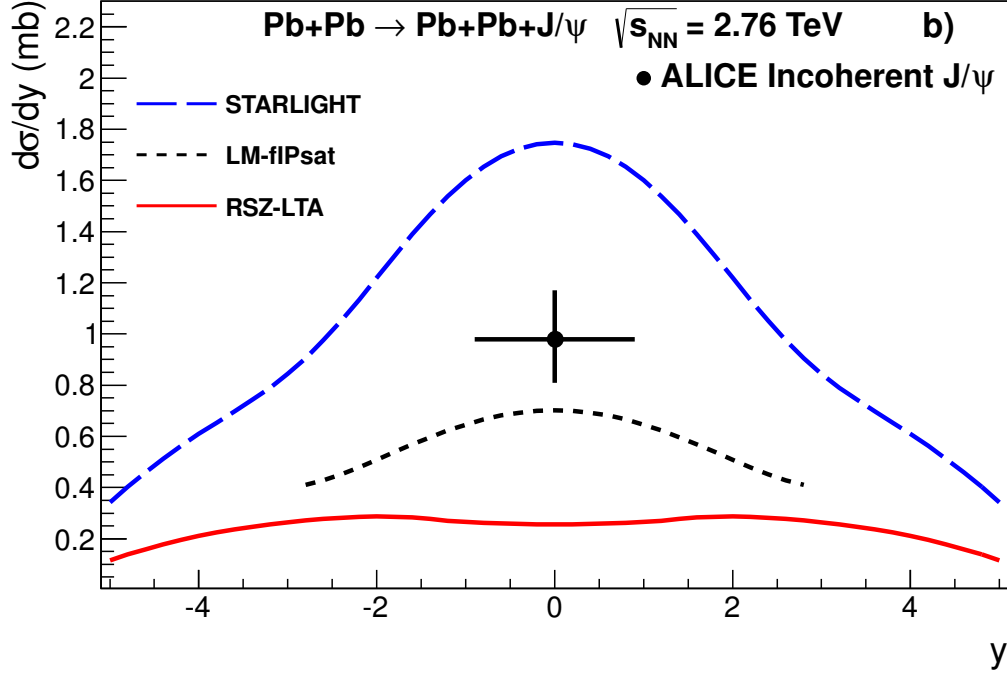
Figure 4.3: Measured differential cross section of J/ψ photoproduction in ultra-peripheral Pb-Pb collisions at $\sqrt{s_{NN}} = 2.76$ TeV at $-0.9 < y < 0.9$ for incoherent events. The error is the quadratic sum of the statistical and systematic errors. The theoretical calculations are also shown [2].

channel.

- The slope of the invariant mass distribution should be consistent with QED two-body scattering falling off as a function of mass with the characteristic E^{-4} ($E \simeq M$, where E is the total energy of the pair and M its invariant mass).

- Observation that the production rate peaks at low pair transverse momentum ($P_\perp$) characteristic of photon collisions generated by the Lorentz-boosted Coulomb field.

- The individual $e^\pm$ particles should be preferentially aligned longitudinally and the azimuthal angle between the e^+e^- pair momentum and the individual $e^\pm$ momenta should display modulations due to the spin states for real photons.

- The measured kinematic distributions should match a theory calculation of the exclusive Breit-Wheeler process without explicit photon virtuality and without employing any higher order corrections.

The used triggering system selects UPC events that may contain only e^+e^- pairs by selecting an interaction in combination with the excitation of the passing nuclei following their dissociation. For nuclear dissociation events two Zero Degree Calorimeters (ZDC) were used and events were classified depending on the number of neutrons in each ZDC. The UPC trigger was configured with an energy threshold
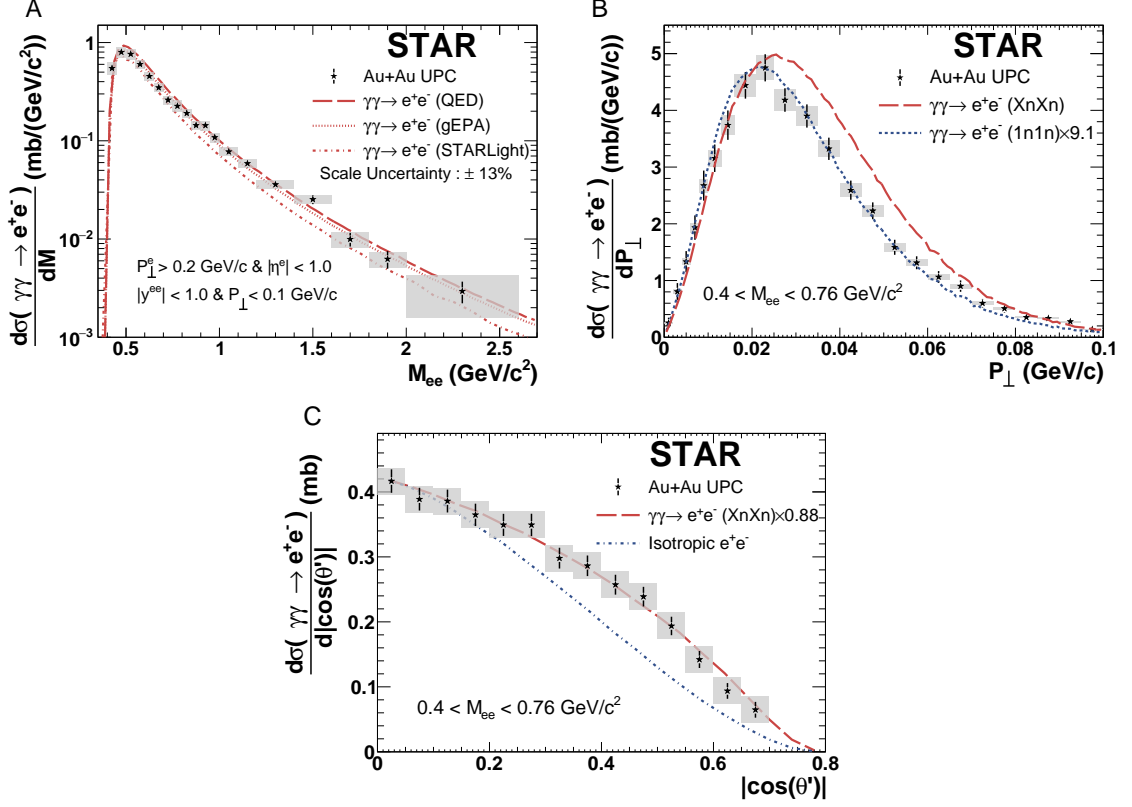
Figure 4.4: The differential cross-section with respect to M_{ee} **(A)**, $P_\perp$ **(B)**, and $|\cos\theta'|$ **(C)** in UPCs. The cross-sections are reported for events with any combination of neutron breakup (XnXn). Since the $P_\perp$ shape depends on the impact parameter, theory curves for the (1n1n) and the (XnXn) cases are shown [5].

resulting in an inefficiency whenever more than 3 neutrons hit one of the ZDCs.

Not only exclusive e^+e^- pair measurements were produced, but also $60-80\%$ central hadronic heavy-ion collisions with impact parameter between approximately 11.5 and 13.5 fm.

The reported total cross section for exclusive e^+e^- pairs is 0.261 ± 0.004 (sta.) ± 0.013 (sys.) ± 0.034 mb with an invariant mass of $0.4 < M_{ee} < 2.6$ GeV/c^2 and with $P_\perp < 0.1$ GeV/c for events with one or more neutron in each ZDC. Comparisons of the measured cross section and three theoretical predictions are shown in Tab. 4.2. The measured total cross section is in good agreement with all theoretical predictions. Productions rates for exclusive e^+e^- pairs are shown in Fig. 4.4 as a function of different variables. Figure Fig. 4.4A shows a smooth invariant mass spectrum with a low-mass cutoff at $M_{ee} \approx 0.4$ GeV/c^2 and with $P_\perp < 100$ MeV/c. The smoothness of the spectrum indicates good purity of the selected UPC events and e^+e^- pair identification and is in good agreement with the expected shape for Breit-Wheeler process. Figure Fig. 4.4B shows the cross section as a function of $P_\perp$ with an invariant mass $0.4 < M_{ee} < 0.76$ GeV/c^2 and with a peak at low pair transverse momentum expected for the Breit-Wheeler process. Figure Fig. 4.4C shows the absolute value of the $\cos\theta'$ distribution, where θ' is the polar angle of the positron momentum vector.
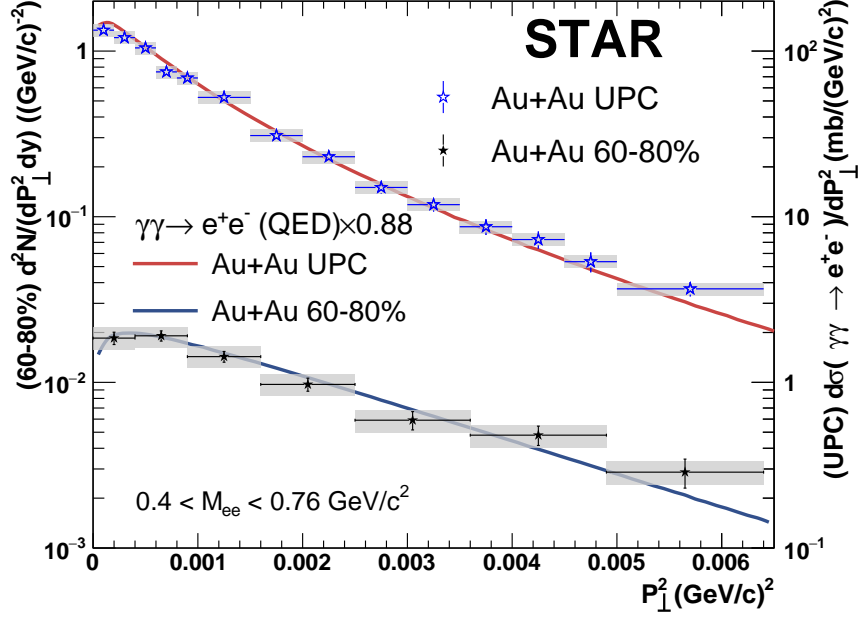
Figure 4.5: Comparison of the $P_\perp^2$ distribution in $60 - 80\%$ central Au+Au collisions with that in UPCs. Statistical uncertainties are shown with vertical bars. Systematic uncertainties are shown with shaded boxes [5].

The paper furthermore compares kinematic distributions of e^+e^- pairs from UPC and central Au+Au measurements. These comparisons are shown in figures Fig. 4.5 and Fig. 4.6. The first figure shows a comparison of the pair transverse momentum squared. The second figure shows a comparison of the $\Delta\phi = \phi_{ee} - \phi_e$ distribution, where ϕ_{ee} and ϕ_e are the azimuthal angle of the momentum in the laboratory frame of the e^+e^- pair and positron respectively. This modulation in the distribution of the azimuthal angle is theoretically predicted for collisions of linearly polarized photons. The showed distributions are for pairs with $P_\perp < 100$ MeV$/c$ and $0.45 < M_{ee} < 0.76$ GeV$/c^2$. Measured distributions are both fit to a function defined as Eq. (4.3) [5], where C is a constant and $A_{2\Delta\phi}$ and $A_{4\Delta\phi}$ are the magnitudes of the $\cos 2\Delta\phi$ and $\cos 4\Delta\phi$ modulations respectively.

$$f(\Delta\phi) = C(1 + A_{2\Delta\phi} \cos 2\Delta\phi + A_{4\Delta\phi} \cos 4\Delta\phi). \tag{4.3}$$

The observed magnitudes with uncertainties are reported in Tab. 4.2, where the $\cos 4\Delta\phi$ modulation is significant, in UPCs with 6.7σ significance.

Total Cross-section	Measured		STARLight	gEPA	QED
$\sigma(\gamma\gamma \to e^+e^-)$ mb	0.261 ± 0.004 (stat.) ± 0.013 (syst.) ± 0.034 (scale)		0.22	0.26	0.29

Differential Quantities	Ultra-Peripheral			Peripheral HHICs		
	Measured	QED	χ^2/ndf	Measured	QED	χ^2/ndf
$|A_{4\Delta\phi}|$ (%)	16.8 ± 2.5	22	18.8 / 16	27 ± 6	39	10.2 / 17
$|A_{2\Delta\phi}|$ (%)	2.0 ± 2.4	0	18.8 / 16	6 ± 6	0	10.2 / 17
$\sqrt{\langle P_\perp^2 \rangle}$ (MeV/c)	38.1 ± 0.9	37.6	—	50.9 ± 2.5	48.5	—

Table 4.2: The top row reports the total measured cross section within STAR acceptance for $\gamma\gamma \to e^+e^-$ in (XnXn) events compared with three theory calculations. The lower rows report measurements of $\Delta\phi$ and $\sqrt{\langle P_\perp^2 \rangle}$ from UPCs and peripheral hadronic heavy-ion collisions with the corresponding theory calculations where applicable. The uncertainties reported here are the statistical and systematic uncertainties added in quadrature [5].
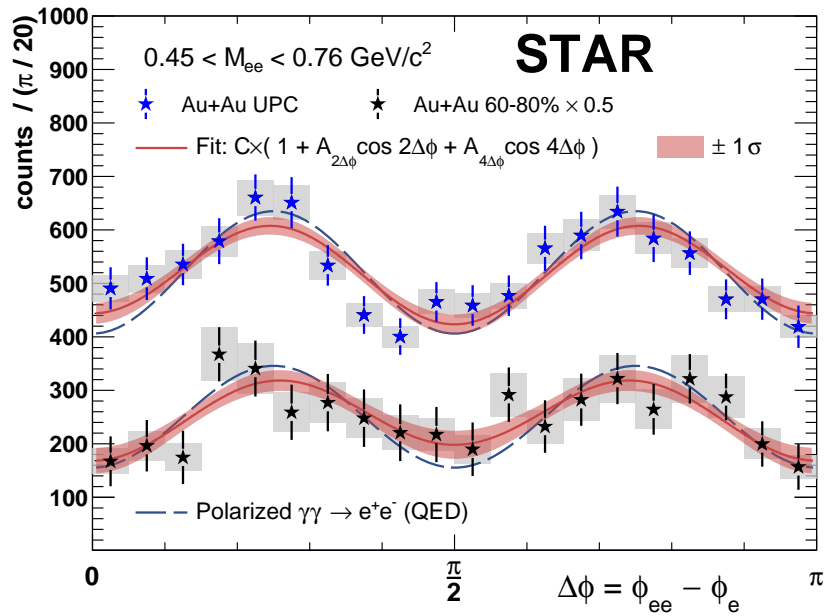
33

Figure 4.6: Comparison of the $\Delta\phi = \phi_{ee} - \phi_e$ distribution from $60-80\%$ central Au+Au collisions with that in UPCs. The $\cos 4\Delta\phi$ modulation extracted from a fit to the $\Delta\phi$ distribution is shown along with the $\pm 1\sigma$ uncertainty band [5].

Chapter 5

Data analysis

My analysis of azimuthal asymmetries of coherent photoproduction of J/ψ at mid-rapidity in ultra-peripheral collisions is presented in this chapter. The presented data were measured at the LHC. The analysed collisions are Pb-Pb collisions at a centre-of-mass energy $\sqrt{s_{NN}} = 5.02$ TeV measured during periods LHC18q and LHC18r. Each period has a different polarity of the L3 magnet. Data from both periods are merged.

5.1   Data selection

In the primary analysis of the data, only events with two good central tracks were selected. This was achieved by putting criteria to both TPC and SPD detectors. The criteria for the TPC detector, to yield a good track, the tracks has to satisfy criterion TestFilterBit (1≪5), which requires that out of a maximum of 159 space points in the TPC, each tracks has at least 70 of those points in the TPC and χ^2/ndf from the Kalman fit is better than 4. Both first and second track have at least one hit in the SPD. The criterion for SPD is HasPointOnITSLayer(0) && HasPointInITSLayer(1) which requires to have hits in the two innermost SPD layers of the detector.

In the secondary analysis several triggers were used:

- For events with run number below 295881 the CCUP31-B-NOPF-CENTNOTRD trigger was used, where NOPF denotes operation with no past-future protection, for higher run numbers the trigger CCUP31-B-SPD2-CENTNOTRD was used with SPD2 past-future protection.

- The reconstructed invariant mass of the dilepton is between 2.2 and 4.5 GeV/c^2.

- AD and V0 offline veto (ADA, ADC, V0A, V0C detectors have to be empty).

- To exclude potential border effects, the dilepton rapidity has to be $|y| < 0.8$.

- The pseudorapidity of both tracks is $|\eta| < 0.8$.

- Only tracks with opposite charges were chosen.

- To choose only muon pairs, the criterion $\sigma^2_{\mu,1} + \sigma^2_{\mu,2} < \sigma^2_{e,1} + \sigma^2_{e,2}$, where $\sigma^2_{\mu(e),i}$ is the distance between the energy loss expected for muon (electron) tracks and the measured energy loss of the track.

The number of remaining events after applying each criterion is listed in Tab. 5.1. The last line of the table lists a criterion applied after the invariant mass distribution cut to choose only J/ψ events, which is important for further analysis.

Selection	Number of remaining events
Two good central tracks	2502214
CCUP31 trigger	2277051
Invariant mass in the interval of (2.2; 4.5) GeV/c^2	54758
ADA offline veto	54548
ADC offline veto	54390
V0A offline veto	46858
V0C offline veto	42259
Dilepton rapidity $y < |0.8|$	41603
Track pseudorapidity $\eta < |0.8|$	33278
Tracks have opposite charges	30144
Muon pairs only	19478
Transverse momentum cut $p_t < 0.2$ Gev/c	12537
Invariant mass in the interval of (3.0; 3.2) GeV/c^2	4055

Table 5.1: Table listing number of remaining events passing the criteria mentioned above.

5.2   AD an V0 decisions

Figures Fig. 5.1 and Fig. 5.2 show two dimensional histograms of AD and V0 detector decisions, where the colour scale is set as logarithmic scale. These histograms provide information about the number of events passing the defined criteria, where 0 means there is no signal in the detector, 1 means there is only signal in the time window corresponding to the beam-beam interactions, number 2 says, that the signal is in the time window corresponding to the beam-gas interactions and 3 corresponds to fake signals. The demanded criteria in this thesis are, that both V0 and AD detectors are empty. This is chosen to reject fake events and possible background. One can see, that most of the measured events are in the bin corresponding to no signal in either detector, showing that the majority of measured events is compatible with no signals in the forward direction.

5.3   Invariant mass distribution

The invariant mass distribution was plotted after applying the data selection mentioned above, that is crucial to choose only coherent events where opposite sign muon pairs are created. The invariant mass distribution shows a peak around 3.1 GeV/c^2. The previously measured mass of J/ψ is $M_{J/\psi} = 3.096916 \pm 0.000011)$
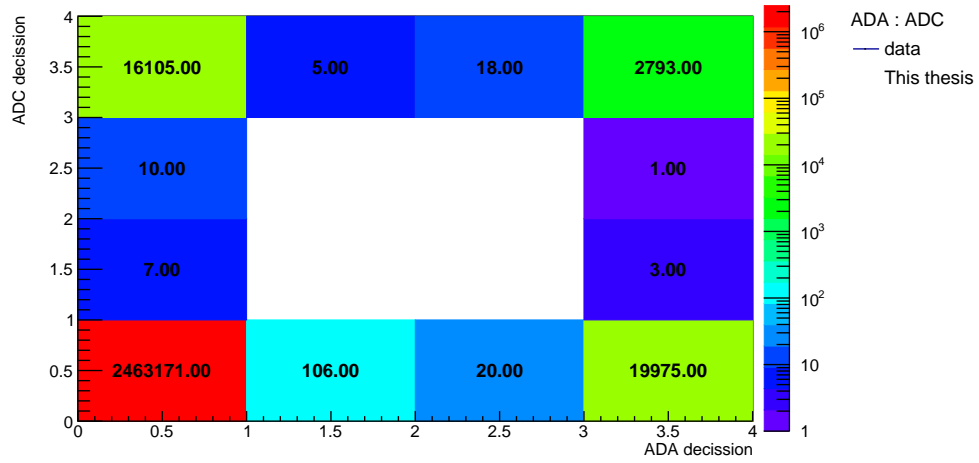
Figure 5.1: Two dimensional histogram of the AD detector decision.
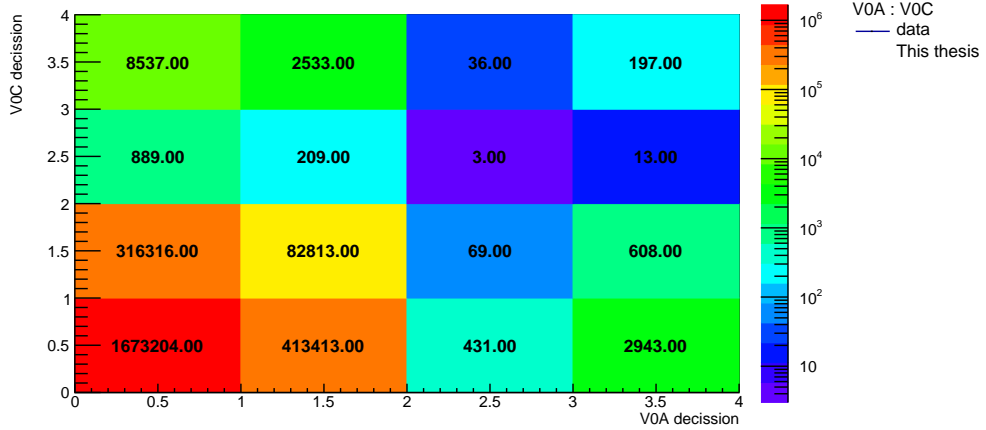

Figure 5.2: Two dimensional histogram of the V0 detector decision.

GeV/c^2 [17]. Given the clear J/ψ peak, another selection was applied to choose only events regarding the J/ψ coherent photoproduction. The plot of the invariant mass distribution is shown in Fig. 5.3.

5.4 Kinematic distributions of muon tracks

Plots of the transverse momentum distribution of positive and negative track are shown in Fig. 5.4 and Fig. 5.5, where the y-axis is set in logarithmic scale. Two dimensional histogram of those tracks is shown in Fig. 5.6 showing that the measured transverse momenta of each track have similar values as expected from the decay of J/ψ at mid-rapidity and with very small transverse momentum.

Figures Fig. 5.7 and Fig. 5.8 show the pseudorapidity distribution of the positive and negative track respectively. Figure Fig. 5.9 shows a two dimensional histogram of those distributions. Pseudorapidity can be used to determine the distribution of the produced particles regarding the polar angle. The two dimensional histogram shows that the data from both distributions are uncorrelated and the produced particles
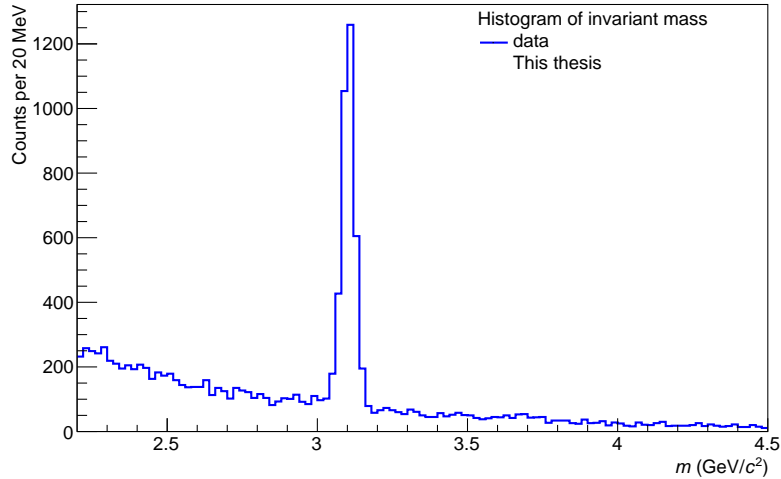
Figure 5.3: Invariant mass distribution of measured dimuon tracks with a clear J/ψ peak.
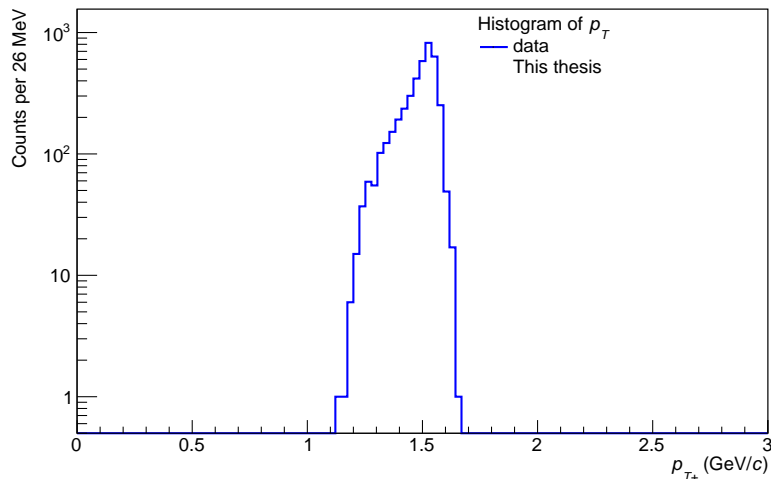

Figure 5.4: Measured transverse momentum distribution of the positive track in the mass interval of $m \in (3.0, 3.2) \mathrm{GeV}/c^2$.

are evenly distributed along the beam.

The measured distributions of azimuthal of the positive and negative track are shown in Fig. 5.10 and Fig. 5.11 respectively. As well as pseudorapidity, the azimuthal angle provides information about particle distribution inside the detector. The two dimensional histogram shown in Fig. 5.12 shows that the produced particles are back-to-back in azimuth. This is a strong indication that these particles originate from a particle with almost zero transverse momentum.

5.5   Azimuthal asymmetry

The plot of the modulation in azimuthal angle is shown in Fig. 5.13. The modulation was calculated by finding the difference in azimuth between two Lorentz vectors obtained from the sum and the difference of the 4-momenta of the tracks. The result
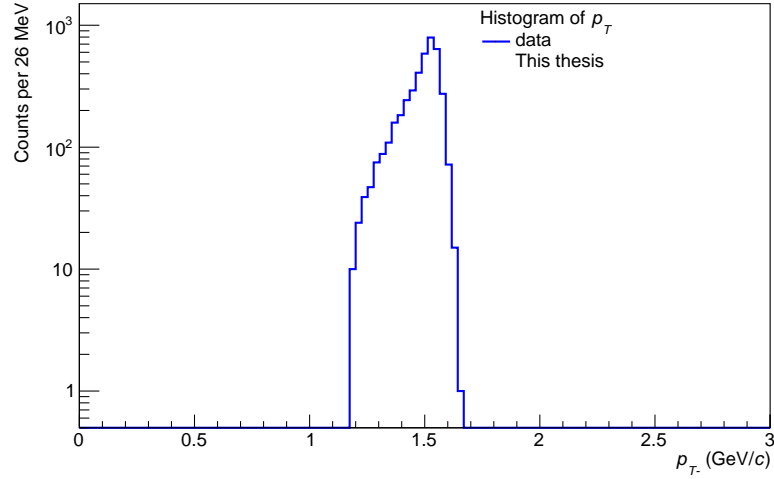
Figure 5.5: Measured transverse momentum distribution of the negative track in the mass interval of $m \in (3.0, 3.2)\text{GeV}/c^2$.
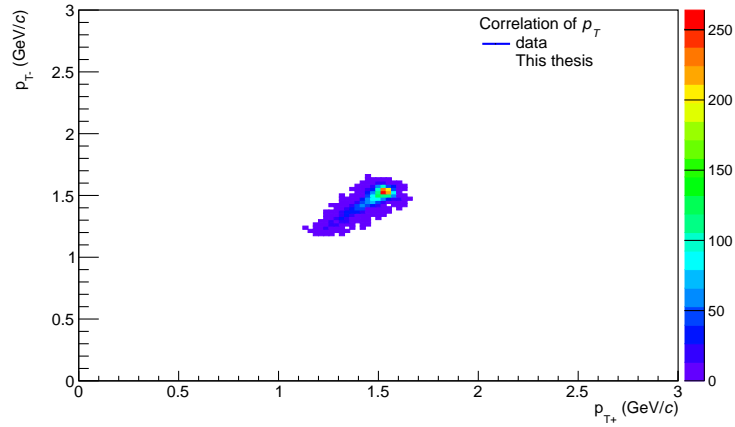

Figure 5.6: Two dimensional histogram of transverse momenta of measured tracks.
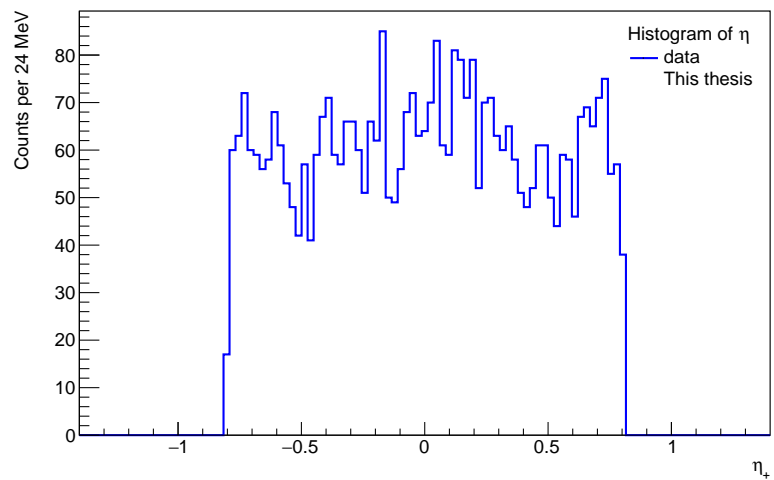

Figure 5.7: Measured pseudorapidity distribution of the positive track in the mass interval of $m \in (3.0, 3.2)\text{GeV}/c^2$.

of this difference was fitted with Eq. (5.1).
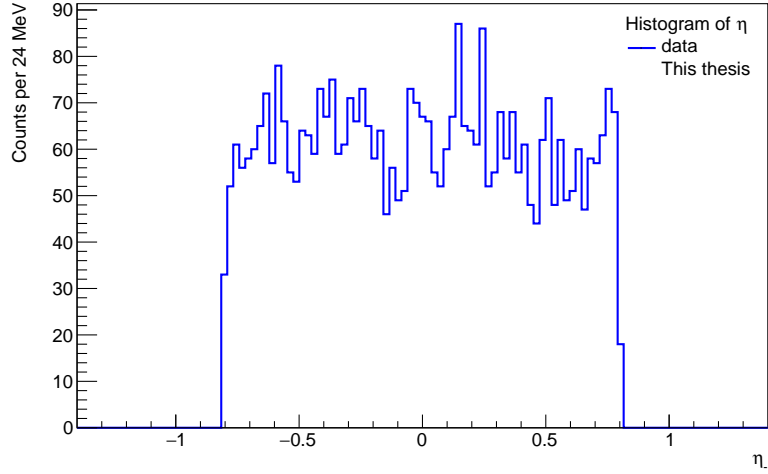
$$f(x) = A + B\cos 2\Delta\phi. \tag{5.1}$$

39

Figure 5.8: Measured pseudorapidity distribution of the negative track in the mass interval of $m \in (3.0, 3.2)\mathrm{GeV}/c^2$.
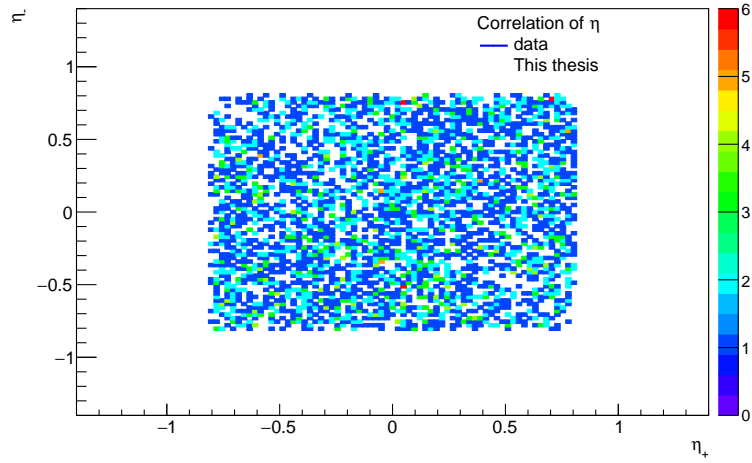

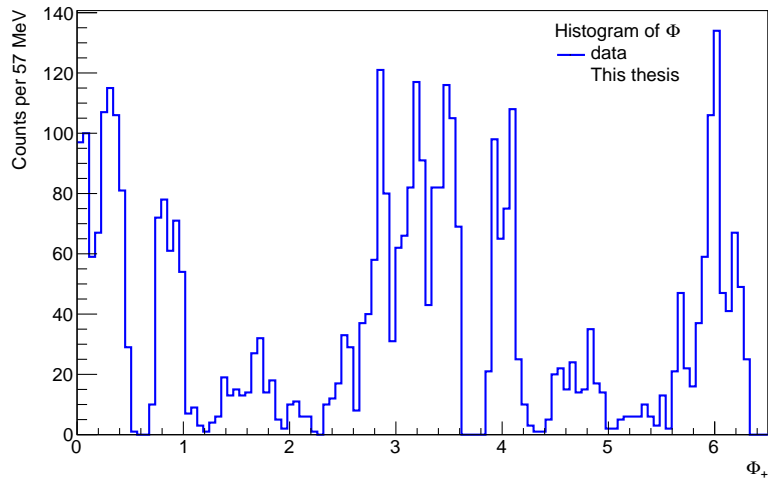**Figure 5.9:** Two dimensional histogram of pseudorapidity of measured tracks.

Figure 5.10: Measured azimuthal angle distribution of the positive track in the mass interval of $m \in (3.0, 3.2)\mathrm{GeV}/c^2$.
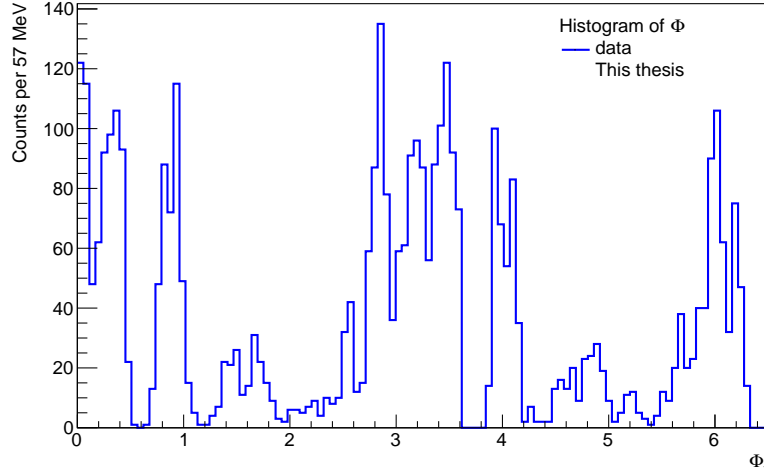
Figure 5.11: Measured azimuthal angle distribution of the negative track in the mass interval of $m \in (3.0, 3.2) \mathrm{GeV}/c^2$.
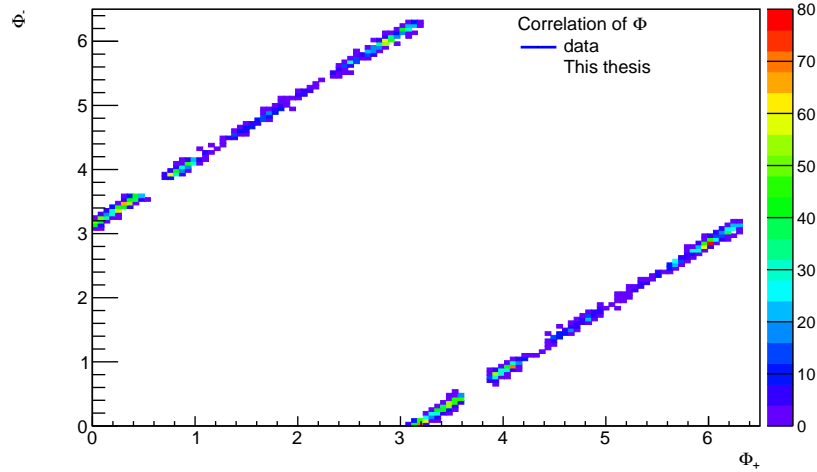

Figure 5.12: Two dimensional histogram of azimuthal angle of measured tracks.

Parameters A and B were obtained by the fit with results shown in Tab. 5.2. The

Parameter	Value
A	43.54 ± 0.70
B	0.128 ± 0.023

Table 5.2: Values of parameters of the fitting function Eq. (5.1).

obtained value of χ^2/ndf is approximately 1.5.

The observed asymmetry is observed at the detector level. One has to take into account the detector effects and make corrections. As shown in figures Fig. 5.10 and Fig. 5.11 the detector effects are important in the azimuth direction.

If the asymmetry remains after corrections, it would be the first observation of this effect. The origin of the modulation and its relation to low-x physics is not completely clear. It seems that the modulation is related to the polarisation of photons in the flux and of the J/ψ. As the two nuclei collide, there are two sources of photons,
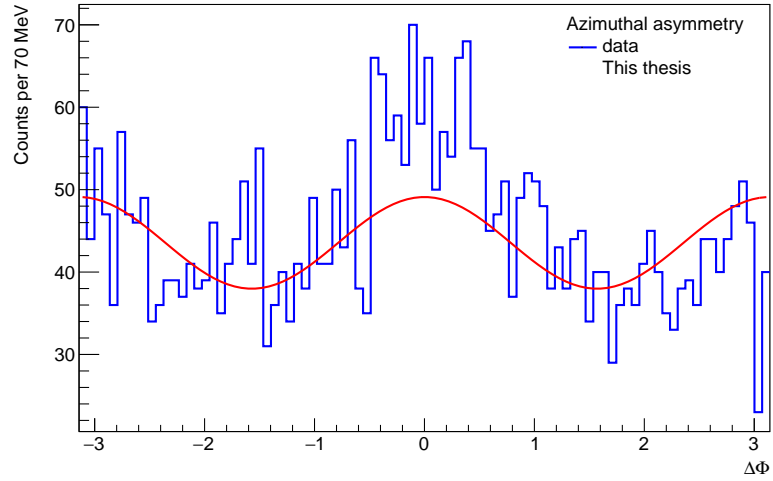
Figure 5.13: The plot of modulation in azimuthal angle with fitting function Eq. (5.1).

that are in case of ultra-relativistic nuclei expected to be linearly polarized, and the interference of those two contributions plays a key role. Further information is being studied and worked out by theoretical scientists. One can see for example [21].

Summary

The aim of this thesis was to asses a possible modulation in azimuthal angle in coherent photoproduction of J/ψ.

In the first chapter the Standard Model is introduced. Firstly the types of particles and their properties crucial for the purposes of this thesis are introduced. The J/ψ is introduced herein with its crucial properties. Furthermore the interactions according to the Standard Model are introduced.

Further in the second chapter the basics of the theory of QCD are mentioned, to present some of the properties of the strong interaction and its mediators gluons. This chapter also explains crucial phenomena related to the gluon structure of hadrons and deep-inelastic scattering, which is a good instrument for probing the structure of hadrons. Related to DIS, the Bjorken scaling and structure functions are mentioned, along with saturation, as those are important terms for understanding the structure of hadrons. What is more, the UPCs are defined here including photoproduction with focus on exclusive vector meson production.

Afterwards the ALICE detector at the LHC is presented, along with a small introduction to CERN and the properties of the LHC. Several parts of the ALICE detector are mentioned, with focus on the key detectors for measurements of the coherent photoproduction. Moreover the data acquisition system is introduced.

Before presenting the measured data, two papers regarding previous measurements are presented. The first paper focuses in the photoproduction of J/ψ and e^+e^- pairs in ultra-peripheral Pb-Pb collisions. The second paper focuses on the probing of the extreme electromagnetic fields with the Breit-Wheeler process, showing a significant $\cos\Delta\phi$ modulation in azimuthal angle.

In the last chapter the results of my analysis are presented along with the criteria applied on the data, to choose only events regarding the coherent photoproduction of J/ψ. The total number of measured J/ψ particles after applying the criteria and choosing only a clear peak in invariant mass distribution is 4055. The kinematic variables of muon tracks and their distributions are presented. The plot of modulation in azimuthal angle shows a possible $\cos\Delta\phi$ modulation in coherent J/ψ photoproduction. Nonetheless further analysis is needed to reduce possible background or errors caused by the detector inefficiency.

Bibliography

[1] K. Aamodt et al. "The ALICE experiment at the CERN LHC". In: *JINST* 3 (2008), S08002. DOI: 10.1088/1748-0221/3/08/S08002.

[2] E. Abbas et al. "Charmonium and e^+e^- pair photoproduction at mid-rapidity in ultra-peripheral Pb-Pb collisions at $\sqrt{s_{NN}}$=2.76 TeV". In: *Eur. Phys. J. C* 73.11 (2013), p. 2617. DOI: 10.1140/epjc/s10052-013-2617-1. arXiv: 1305.1467 [nucl-ex].

[3] *About CERN | CERN*. URL: https://alice.cern/node/5011 (visited on 03/20/2021).

[4] Jaroslav Adam. "Photoproduction of J/ψ in ultra-peripheral p-Pb and Pb-Pb collisions with the ALICE detector at the LHC". PhD thesis. Prague, Tech. U., May 2016.

[5] Jaroslav Adam et al. "Probing Extreme Electromagnetic Fields with the Breit-Wheeler Process". In: (Oct. 2019). arXiv: 1910.12400 [nucl-ex].

[6] J. Adolfsson et al. "The upgrade of the ALICE TPC with GEMs and continuous readout". In: *JINST* 16.03 (2021), P03022. DOI: 10.1088/1748-0221/16/03/P03022. arXiv: 2012.09518 [physics.ins-det].

[7] Ramon Cid Manzano Cabier Cid Vidal. *Taking a closer look at LHC - LHC running*. URL: http://lhc-closer.es/taking_a_closer_look_at_lhc/0.lhc_running (visited on 03/20/2021).

[8] F. Carena et al. "The ALICE data acquisition system". In: *Nucl. Instrum. Meth. A* 741 (2014), pp. 130–162. DOI: 10.1016/j.nima.2013.12.015.

[9] S. Chekanov et al. "ZEUS next-to-leading-order QCD analysis of data on deep inelastic scattering". In: *Physical Review D* 67.1 (Jan. 2003). ISSN: 1089-4918. DOI: 10.1103/physrevd.67.012007. URL: http://dx.doi.org/10.1103/PhysRevD.67.012007.

[10] J. G. Contreras and J. D. Tapia Takaki. "Ultra-peripheral heavy-ion collisions at the LHC". In: *Int. J. Mod. Phys. A* 30 (2015), p. 1542012. DOI: 10.1142/S0217751X15420129.

[11] H1 and ZEUS Collaborations. *Combination of Measurements of Inclusive Deep Inelastic $e^\pm p$ Scattering Cross Sections and QCD Analysis of HERA Data*. 2015. arXiv: 1506.06042 [hep-ex].

[12] Julie Haffner. "The CERN accelerator complex. Complexe des accélérateurs du CERN". In: (Oct. 2013). General Photo. URL: http://cds.cern.ch/record/1621894.

[13] G. Herrera-Corral. "Diffractive Physics with ALICE at the LHC: the control of quantum collisions". In: *Journal of Physics: Conference Series* 624 (June 2015), p. 012008. DOI: `10.1088/1742-6596/624/1/012008`. URL: `https://doi.org/10.1088/1742-6596/624/1/012008`.

[14] V. Alan Kostelecký, E. Lunghi, and A.R. Vieira. "Lorentz violation and deep inelastic scattering". In: *Physics Letters B* 769 (2017), pp. 272–280. ISSN: 0370-2693. DOI: `https://doi.org/10.1016/j.physletb.2017.03.047`. URL: `https://www.sciencedirect.com/science/article/pii/S0370269317302356`.

[15] I.V. Kotov. "Inner tracking system of the ALICE experiment. Overview". In: *Nuclear Instruments and Methods in Physics Research Section A: Accelerators, Spectrometers, Detectors and Associated Equipment* 568.1 (2006). New Developments in Radiation Detectors, pp. 274–276. ISSN: 0168-9002. DOI: `https://doi.org/10.1016/j.nima.2006.07.019`. URL: `https://www.sciencedirect.com/science/article/pii/S0168900206012721`.

[16] *More details on the ALICE V0 detector | CERN Alice*. URL: `https://alice.cern/node/5535` (visited on 03/20/2021).

[17] K.A. Olive. "Review of Particle Physics". In: *Chinese Physics C* 38.9 (Aug. 2014), p. 090001. DOI: `10.1088/1674-1137/38/9/090001`. URL: `https://doi.org/10.1088/1674-1137/38/9/090001`.

[18] "Performance of the ALICE experiment at the CERN LHC". In: *International Journal of Modern Physics A* 29.24 (Sept. 2014), p. 1430044. ISSN: 1793-656X. DOI: `10.1142/s0217751x14300440`. URL: `http://dx.doi.org/10.1142/S0217751X14300440`.

[19] Kyrre Skjerdal. "Photoproduction of $\rho0$ in ultra–peripheral nuclear collisions at ALICE". In: *Journal of Physics: Conference Series* 455 (Aug. 2013), p. 012010. ISSN: 1742-6596. DOI: `10.1088/1742-6596/455/1/012010`. URL: `http://dx.doi.org/10.1088/1742-6596/455/1/012010`.

[20] Wikipedia. *Large Hadron Collider - Wikipedia*. URL: `https://en.wikipedia.org/wiki/Large_Hadron_Collider` (visited on 03/20/2021).

[21] Wangmei Zha et al. "Exploring the double-slit interference with linearly polarized photons". In: *Phys. Rev. D* 103.3 (2021), p. 033007. DOI: `10.1103/PhysRevD.103.033007`. arXiv: `2006.12099 [hep-ph]`.